

# **C**old Leg Mixing Computational Fluid Dynamics – Uncertainty Quantification (CLM-UQ) Benchmark Results



**NUCLEAR ENERGY AGENCY  
COMMITTEE ON THE SAFETY OF NUCLEAR INSTALLATIONS**

**Cold leg mixing computational fluid dynamics – uncertainty quantification  
(CLM-UQ) benchmark results**

This document is available in PDF format only.

**JT03505057**

## ORGANISATION FOR ECONOMIC CO-OPERATION AND DEVELOPMENT

The OECD is a unique forum where the governments of 38 democracies work together to address the economic, social and environmental challenges of globalisation. The OECD is also at the forefront of efforts to understand and to help governments respond to new developments and concerns, such as corporate governance, the information economy and the challenges of an ageing population. The Organisation provides a setting where governments can compare policy experiences, seek answers to common problems, identify good practice and work to co-ordinate domestic and international policies.

The OECD member countries are: Australia, Austria, Belgium, Canada, Chile, Colombia, Costa Rica, the Czech Republic, Denmark, Estonia, Finland, France, Germany, Greece, Hungary, Iceland, Ireland, Israel, Italy, Japan, Korea, Latvia, Lithuania, Luxembourg, Mexico, the Netherlands, New Zealand, Norway, Poland, Portugal, the Slovak Republic, Slovenia, Spain, Sweden, Switzerland, Türkiye, the United Kingdom and the United States. The European Commission takes part in the work of the OECD.

OECD Publishing disseminates widely the results of the Organisation's statistics gathering and research on economic, social and environmental issues, as well as the conventions, guidelines and standards agreed by its members.

## NUCLEAR ENERGY AGENCY

The OECD Nuclear Energy Agency (NEA) was established on 1 February 1958. Current NEA membership consists of 34 countries: Argentina, Australia, Austria, Belgium, Bulgaria, Canada, the Czech Republic, Denmark, Finland, France, Germany, Greece, Hungary, Iceland, Ireland, Italy, Japan, Korea, Luxembourg, Mexico, the Netherlands, Norway, Poland, Portugal, Romania, Russia (suspended), the Slovak Republic, Slovenia, Spain, Sweden, Switzerland, Türkiye, the United Kingdom and the United States. The European Commission and the International Atomic Energy Agency also take part in the work of the Agency.

The mission of the NEA is:

- to assist its member countries in maintaining and further developing, through international co-operation, the scientific, technological and legal bases required for a safe, environmentally sound and economical use of nuclear energy for peaceful purposes;
- to provide authoritative assessments and to forge common understandings on key issues as input to government decisions on nuclear energy policy and to broader OECD analyses in areas such as energy and the sustainable development of low-carbon economies.

Specific areas of competence of the NEA include the safety and regulation of nuclear activities, radioactive waste management and decommissioning, radiological protection, nuclear science, economic and technical analyses of the nuclear fuel cycle, nuclear law and liability, and public information. The NEA Data Bank provides nuclear data and computer program services for participating countries.

This document, as well as any data and map included herein, are without prejudice to the status of or sovereignty over any territory, to the delimitation of international frontiers and boundaries and to the name of any territory, city or area.

Corrigenda to OECD publications may be found online at: [www.oecd.org/about/publishing/corrigenda.htm](http://www.oecd.org/about/publishing/corrigenda.htm).

### © OECD 2022

You can copy, download or print OECD content for your own use, and you can include excerpts from OECD publications, databases and multimedia products in your own documents, presentations, blogs, websites and teaching materials, provided that suitable acknowledgement of the OECD as source and copyright owner is given. All requests for public or commercial use and translation rights should be submitted to [neapub@oecd-nea.org](mailto:neapub@oecd-nea.org). Requests for permission to photocopy portions of this material for public or commercial use shall be addressed directly to the Copyright Clearance Center (CCC) at [info@copyright.com](mailto:info@copyright.com) or the Centre français d'exploitation du droit de copie (CFC) [contact@cfcopies.com](mailto:contact@cfcopies.com).

---

---

## *COMMITTEE ON THE SAFETY OF NUCLEAR INSTALLATIONS*

The Committee on the Safety of Nuclear Installations (CSNI) addresses Nuclear Energy Agency (NEA) programmes and activities that support maintaining and advancing the scientific and technical knowledge base of the safety of nuclear installations.

The Committee constitutes a forum for the exchange of technical information and for collaboration between organisations, which can contribute, from their respective backgrounds in research, development and engineering, to its activities. It has regard to the exchange of information between member countries and safety R&D programmes of various sizes in order to keep all member countries involved in and abreast of developments in technical safety matters.

The Committee reviews the state of knowledge on important topics of nuclear safety science and techniques and of safety assessments, and ensures that operating experience is appropriately accounted for in its activities. It initiates and conducts programmes identified by these reviews and assessments in order to confirm safety, overcome discrepancies, develop improvements and reach consensus on technical issues of common interest. It promotes the co-ordination of work in different member countries that serve to maintain and enhance competence in nuclear safety matters, including the establishment of joint undertakings (e.g. joint research and data projects), and assists in the feedback of the results to participating organisations. The Committee ensures that valuable end-products of the technical reviews and analyses are provided to members in a timely manner, and made publicly available when appropriate, to support broader nuclear safety.

The Committee focuses primarily on the safety aspects of existing power reactors, other nuclear installations and new power reactors; it also considers the safety implications of scientific and technical developments of future reactor technologies and designs. Further, the scope for the Committee includes human and organisational research activities and technical developments that affect nuclear safety.

## *Acknowledgements*

The Nuclear Energy Agency (NEA) Committee on the Safety of Nuclear Installations (CSNI) and the Working Group on the Analysis and Management of Accidents (WGAMA), wish to acknowledge the significant contributions of those individuals who had a key role in the preparation of the summary report, and those who had a leadership role in the conduct and success of the NEA benchmark on “Cold leg mixing computational fluid dynamics – uncertainty quantification (CLM-UQ)”. Additional thanks are extended to D. Bestion, G. Zigh, P. Freydier, P. Ruyer, in support of the CFD Task Group activities.

### *Leading authors*

Rodolfo VAGHETTO	Texas A&M University
Yassin HASSAN	Texas A&M University

### *Contributors*

Satoshi ABE	JAEA
Dominique BESTION	CEA
Romain CAMY	EDF
Andrey DEULIN	ROSATOM
Fabien DUVAL	IRSN
Marc FORESTIER	IRSN
Philippe FREYDIER	EDF
Luka GOLIBRODO	GIDROPRESS
Yassin A. HASSAN	Texas A&M University
Jungwoo KIM	SEOULTECH
Jonathan LAI	Texas A&M University
Erwan LE COUPANEC	EDF
Daniel OREA	Texas A&M University
Yago RIVERA DURAN	UPVAL
Pierre RUYER	IRSN
Dmitrii SVESHNIKOV	OKBM Afrikantov
Rodolfo VAGHETTO	Texas A&M University

Daniele VIVALDI

IRSN

Vasilii VOLKOV

GIDROPRESS

*NEA Secretariat support to the group*

Jeong NAM

NEA

Nils SANDBERG

NEA

## *Table of contents*

<b>Executive summary .....</b>	<b>8</b>
<b>List of abbreviations and acronyms.....</b>	<b>10</b>
<b>1. Introduction .....</b>	<b>11</b>
<b>2. Background.....</b>	<b>12</b>
<b>3. Experimental facility description.....</b>	<b>14</b>
<b>4. Test conditions and measurement locations.....</b>	<b>17</b>
Fluid properties.....	17
Measurement locations .....	19
<b>5. Experimental methods and measurement techniques.....</b>	<b>21</b>
Particle image velocimetry .....	21
Laser induced fluorescence.....	22
LIF calibration .....	22
Experimental method.....	24
<b>6. Uncertainty analysis .....</b>	<b>28</b>
<i>PIV uncertainty</i> .....	28
<i>LIF error sources</i> .....	29
<b>7. Participants and submitted results .....</b>	<b>32</b>
<b>8. Benchmark results.....</b>	<b>34</b>
Cold leg results – Streamwise time-averaged velocity component (CL1 Location) .....	34
Cold leg results – Time-averaged concentrations.....	35
Downcomer results – Streamwise time-averaged velocity component (DC1 Location).....	38
Downcomer results – Streamwise time-averaged velocity component (DC2 Location).....	41
<b>9. Synthesis and conclusion.....</b>	<b>44</b>
<b>References .....</b>	<b>45</b>

### **Tables**

Table 4.1. Dimensions of vessels and cold leg.....	15
Table 5.1. Fluid properties of sampled mixtures (OT).....	17
Table 5.2. OT and BT fluid properties. ....	19
Table 6.1. Equipment and instrumentation specification .....	27
Table 7.1. Values used for OT and BT uncertainty analysis.....	29
Table 9.1. Time-averaged measured quantities.....	34

## Figures

Figure 1.1. Vessel and Cold Leg Geometry .....	8
Figure 4.1. Experimental facility and instrumentation.....	14
Figure 4.2. Vessel and cold leg geometry. ....	15
Figure 4.3. Cold leg vessel nozzle.....	16
Figure 5.1. Density vs. refractive index of solutions.....	18
Figure 5.2. Viscosity of fluid mixtures.....	18
Figure 5.3. Visualisation windows relative to the valve centerline.....	19
Figure 6.1. OT and BT LIF 5-point calibration curve from window average intensity. ....	23
Figure 6.2. OT LIF 5-point local calibration curve for a single point in point in space.....	24
Figure 6.3. Camera setup for cold leg window. ....	25
Figure 6.4. Cold Leg Visualisation and Filter Effect .....	26
Figure 6.5. Camera system for simultaneous PIV measurements. ....	26
Figure 7.1. Background intensity distribution.....	30
Figure 7.2. Normalised intensity along horizontal profile. ....	30
Figure 7.3. Normalised intensity along vertical profile.....	31
Table 8.1.Submitted simulation results .....	34
Figure 9.1. Y-position vs. U (cm/s) 5-10 second time-averaged U – CL1 .....	34
Figure 9.2. Y-position vs. U (cm/s) 10-15 second time-averaged U – CL1 .....	35
Figure 9.3. Y-position vs. U (cm/s) 15-22.24 second time-averaged U – CL1 .....	35
Figure 9.4. Y-position vs. concentration (%) 5-10 second time-averaged C – CL1 .....	36
Figure 9.5. Y-position vs. concentration (%) 10-15 second time-averaged C – CL1 .....	36
Figure 9.6. Y-position vs. concentration (%) 15-22.24 second time-averaged C – CL1 .....	37
Figure 9.7. V (cm/s) vs. X-position 10.5-15.5 second time-averaged V – DC1 .....	38
Figure 9.8. V (cm/s) vs. X-position 15.5-20.5 second time-averaged V – DC1 .....	38
Figure 9.9. V (cm/s) vs. X-position 20.5-25.5 second time-averaged V – DC1 .....	39
Figure 9.10. V (cm/s) vs. X-position 25.5-30.5 second time-averaged V – DC1 .....	39
Figure 9.11. V (cm/s) vs. X-position 30.5-35.5 second time-averaged V – DC1 .....	40
Figure 9.12. V (cm/s) vs. X-position 35.5-41.538 second time-averaged V – DC1 .....	40
Figure 9.13. V (cm/s) vs. X-position 10.5-15.5 second time-averaged V – DC2 .....	41
Figure 9.14. V (cm/s) vs. X-position 15.5-20.5 second time-averaged V – DC2 .....	41
Figure 9.15. V (cm/s) vs. X-position 20.5-25.5 second time-averaged V – DC2 .....	42
Figure 9.16. V (cm/s) vs. X-position 25.5-30.5 second time-averaged V – DC2 .....	42
Figure 9.17. V (cm/s) vs. X-position 30.5-35.5 second time-averaged V – DC2 .....	43
Figure 9.18. V (cm/s) vs. X-position 35.5-41.538 second time-averaged V – DC2 .....	43

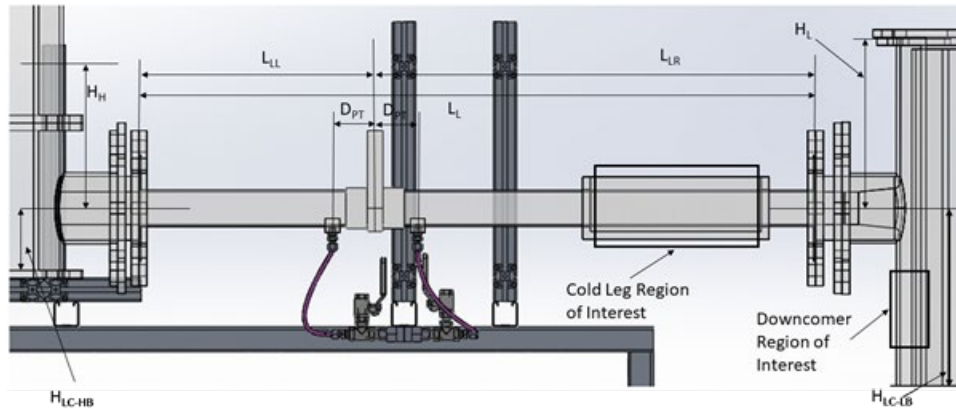
## *Executive summary*

The cold leg mixing computational fluid dynamics (CFD) – uncertainty quantification (CLM-UQ) benchmark is the fifth benchmark concerning CFD applications to nuclear reactor safety to be organised in the framework of the Nuclear Energy Agency (NEA) Working Group on Accident Management and Analysis (WGAMA).

The main objective of this benchmark is to go a step further in the application of single phase CFD to nuclear safety issues involving mixing problems in the presence of buoyancy effects, like pressurised thermal shocks (PTS).

The experiments were performed at Texas A&M University (TAMU). The test facility was designed to simulate mixing phenomena of cold water and hot water in a horizontal cold leg of a pressurised water reactor (PWR), as encountered in some accidental situations like the PTS. The experimental test facility, as shown in Figure 1.1, consists of two large transparent vessels connected through a horizontal acrylic pipe. The vessel on the right represents the reactor pressure vessel of a PWR, and is initially filled with low density water (representing hot water). The vessel on the left is initially filled with heavier water. At time zero, a knife valve in the horizontal leg is rapidly opened and cold water (here represented by the heavier liquid in the left vessel) enters the cold leg and is allowed to flow into the pressure vessel.

**Figure 1.1. Vessel and cold leg geometry**



Source: Orea et al., 2019.

Velocities were measured in the two regions of interest (in the cold leg and in the downcomer). Concentration (and thus water density) was measured in the cold leg.

The benchmark exercise started with 36 participants from 11 countries and 22 institutions. In the end, 19 participants (grouped in 11 teams) from 6 countries and 10 institutions submitted CFD calculation results. The results of the cold leg mixing benchmark were presented at the third meeting that took place at the UIC-P Espace Congrès in Paris (France) on 26 June 2019.

Four teams used the same code (CFX), while each of the other teams used a different CFD code, meaning a total of eight different CFD codes were used. Eight teams used Large Eddy Simulation (LES), while three teams used a Reynolds Averaged Navier-

Stokes (RANS)/Unsteady RANS simulation (URANS) approach as CFD techniques for turbulence modelling.

The number of nodes in the CFD mesh varies between about 200 000 (for the coarsest RANS approach) to about half a billion (for the finest LES). Five teams performed an analysis of uncertainties.

Results obtained in the horizontal leg show that:

- All participants predict a stratification of concentrations (and thus density) in the horizontal leg, but a systematic bias is observed for the vertical concentration profile; in all calculation results, the vertical position of this stratification is lower than the measured position and out of the experimental uncertainty range.
- Most participants predict the correct general shape of the velocity profile as a function of vertical position; the vertical position of the inflexion point (corresponding to zero horizontal velocity at the boundary between the two fluid layers) is globally well predicted.
- There is a significant scattering between participants' results concerning the velocity magnitude in the horizontal leg; most participants predict a velocity magnitude higher than the measured value and out of the experimental uncertainty range; a few are close to the experimental results and one participant predicts a lower magnitude of velocity.

The fact that calculation results give the correct vertical position for the velocity inflexion point, but not for the concentration stratification level, is rather surprising and should be further investigated.

In the downcomer, the comparison of velocity profiles between the inner and outer wall shows significant scattering of calculation results. The difference with experimental results is quite large, except for the LES computations with the largest number of cells, especially at the beginning of the test; this scattering gets lower at later stages of the transient (after 30 s). The difference concerns:

- the vertical flowrate along the measured line, which is related to the prediction of the span width (azimuthal direction along the annulus) of the falling jet;
- the velocity profile shape through the annulus, which directly impacts the prediction capability of the CFD for the gradients along the outer wall of the downcomer, this region being of primary relevance for the corresponding safety application.

A second report, dealing with “open phase” post-test calculations and including further physical analysis of the results, will be issued later.

*List of abbreviations and acronyms*

BT	Blind test
CEA	Commissariat à l'Énergie atomique et aux énergies alternatives (Alternative Energies and Atomic Energy Commission, France)
CFD	Computational fluid dynamics
CLM-UQ	Cold leg mixing computational fluid dynamics – uncertainty quantification
CSNI	Committee on the Safety of Nuclear Installations (NEA)
DPIV	Digital particle image velocimetry
EDF	Électricité de France
HH	Height of Heavy (fluid)
HL	Height of Light (vessel)
IRSN	Institut de Radioprotection et de Sûreté Nucléaire (Institute for Radiological Protection and Nuclear Safety, France)
JAEA	Japan Atomic Energy Agency
LES	Large Eddy Simulation
LIF	Laser induced fluorescence
NEA	Nuclear Energy Agency
OT	Open test
PIV	Particle image velocimetry
PTS	Pressurised thermal shock
PWR	Pressurised water reactor
RANS	Reynolds Averaged Navier-Stokes
RI	Refractive index
RPC	Robust phase correlation
TAMU	Texas A&M University
URANS	Unsteady RANS simulation
WGAMA	Working Group on Accident Management and Analysis (NEA)

## 1. Introduction

The experiments were performed at Texas A&M University (TAMU). The test facility is designed to simulate mixing phenomena of cold water and hot water in a horizontal cold leg of a PWR, as encountered in some accidental situations.

The benchmark exercise started with 36 participants from 11 countries and 22 institutions. In the end, 19 participants from 6 countries and 10 institutions submitted CFD calculation results.

The experimental facility, the test conditions and the measurements are presented below. The calculation results obtained by the 19 participants are then presented and compared to the experimental results.

A second report, dealing with “open phase” post-test calculations and including further physical analysis of the results, will be issued later.

## 2. Background

Computer codes for analysis of the thermal hydraulics of the primary circuit and associated safety systems under postulated accident conditions have traditionally been based on one-dimensional flow models that are fitted and validated against experiments. Since the early 2000s, single phase computational fluid dynamics has been increasingly used for design and safety analysis related to specific aspects of reactor thermal hydraulics. The NEA Working Group for the Analysis and Management of Accidents (WGAMA) has been working over the past 15 years to evaluate the potential of CFD methods to bring additional insight and knowledge, and increased precision, to thermal hydraulics safety analysis. A list of safety issues where CFD may bring additional benefits was established, a best practice guideline was produced, and uncertainty quantification for CFD methods was addressed. In addition, a series of benchmarks was organised in order to evaluate the precision and predictive power of CFD methods for different specific scenarios.

One of the scenarios where CFD has the potential to add crucial new knowledge compared to traditional 1D methods is pressurised thermal shock (PTS). This scenario was selected for the current benchmark exercise because of its safety relevance, and because it represents a case which can be handled by standard CFD codes while at the same time being challenging in terms of geometry and boundary conditions.

More specifically, the scenario for the current benchmark is the following: two tanks are connected by a straight pipe which represents a cold leg and is equipped with a knife valve. One of the tanks represents the pressure vessel, with an annual downcomer installed, while the other tank represents the safety injection tank. At time zero, the knife valve is rapidly opened and cold water (here represented by a heavier liquid) enters the cold leg and is allowed to flow into the pressure vessel. The safety concern is that when the cold leg water enters the pressure vessel, thermal stresses may induce crack initiation/growth, which, in turn could challenge the integrity of the vessel if it happens at elevated pressure.

The conditions of the current benchmark can be compared to reactor conditions as follows: the density difference between the two liquids corresponds roughly to what one would have in a real reactor, and the geometry represents well that of the cold leg and the downcomer despite scaling distortion (approximately a factor of ten). In particular, the actual connection between the two was precisely modelled after a real reactor component. On the other hand, the initial and boundary conditions of the experiment are rather idealised in the sense that initially stagnant heavy fluid is allowed to mix with stagnant light fluid in the cold leg. In an actual safety analysis, one must consider the possibility of much more complex situations with highly dynamic flows usually under two-phase conditions. However, the current scenario can be seen as one possible worst-case scenario, since more turbulent situations than the one studied here will lead to more mixing between cold and hot water, and thereby to lower thermal stresses in the downcomer.

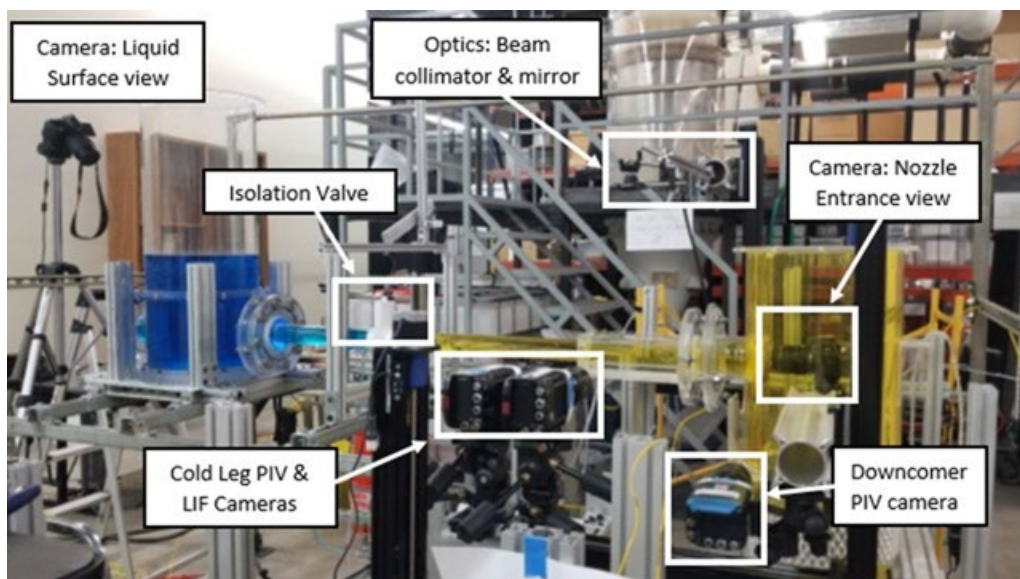
From a modelling perspective, the following aspects of the current benchmark are worth pointing out. First, if a benchmark is to be successful, the initial and boundary conditions need to be well defined. This was repeatedly found in previous benchmarks, and it has been emphasised that measurements in the test section may be highly sensitive not only

to the inlet conditions but also to outlet conditions. For that reason, much attention was given in the current benchmark to make sure that the fluids were completely stagnant at the beginning of the test. Also the influence of the lifting of the knife valve was carefully evaluated. Second, it has been previously found that the density difference between heavy and light fluids may impact measurements that rely on optical instruments if the refractive indices also differ. For that reason, efforts were made to find two liquids with different density but similar refractive indices. This has allowed unprecedented precision to be obtained in the current particle image velocimetry (PIV) measurements of a mixing scenario. Third, the comparatively complex geometry and the time dependence of the current transient scenario present certain challenges. Computationally, the scenario is challenging but clearly within reach for current state-of-the-art CFD calculations. However, to compare calculations with measurements in a meaningful way still presents several difficulties. Averaging times and statistics need to be judiciously selected in order to distinguish between random fluctuations and systematic trends and account for the capabilities of the different methods for resolving turbulence. These aspects were carefully discussed as part of the current benchmark exercise, before deciding on a set of output data to be used as figures of merit.

### 3. Experimental facility description

The experimental test facility consists of two large transparent vessels connected through a horizontal acrylic pipe. One of the vessels is designed to incorporate specific features and the geometry of a typical reactor vessel. The nozzle is constructed to realistically represent the fluid domain of the cold leg nozzle of a PWR vessel. An overview of the experimental facility with the instrumentation installed is provided in Figure 3.1.

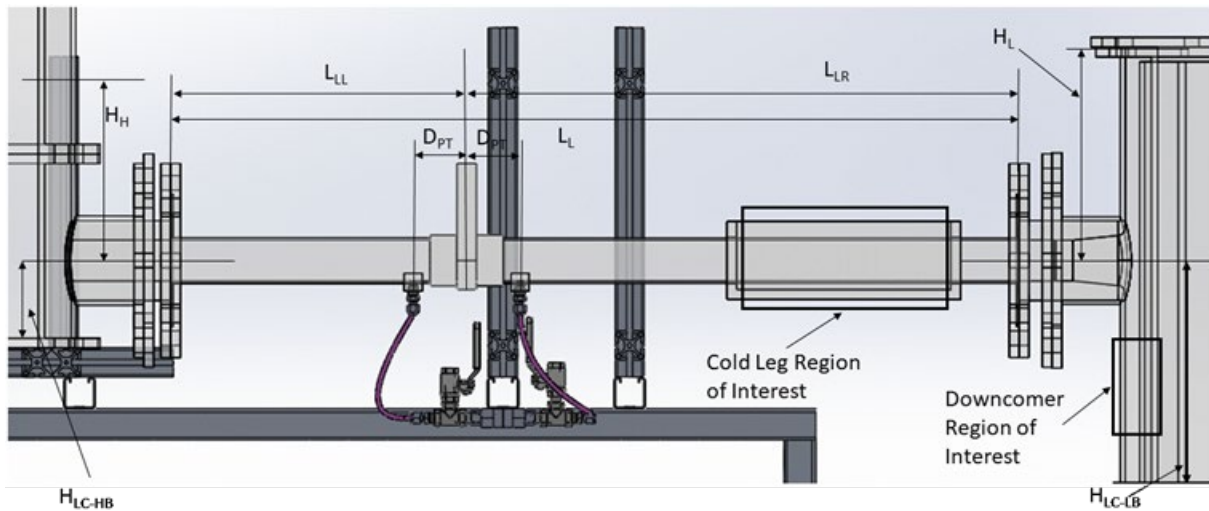
**Figure 3.1. Experimental facility and instrumentation**



Note: blue solution represents the cold/heavier water; yellow solution represents the hot/lighter water.  
Source: Orea et al., 2019.

The vessel on the left is used as a tank for the solution simulating the cold/heavy water injection (blue solution in Figure 3.1), and is initially filled to a predetermined height. This vessel is referred to as the heavy vessel due to the heavier density fluid. The vessel on the right represents the reactor vessel. This is made by two acrylic cylinders, the external cylinder representing the vessel wall and the internal cylinder representing the reactor barrel. The annular region between these cylinders represents the downcomer of the reactor, which is initially filled with a surrogate solution to the hot water (yellow solution in Figure 3.1). This vessel is referred to as the light vessel because of the lower density fluid. An isolation valve is installed within the connecting horizontal leg to keep the two solutions isolated during test preparation. The isolation valve is attached to a spring lever mechanism to achieve consistent and repetitive opening times. Attached to the valve is a switch that is used to trigger the cameras to begin recording when the isolation valve is open. Figure 3.2 and Table 3.1 provide the main dimensions of the heavy, light vessels and the leg that connects the two vessels.

Figure 3.2. Vessel and cold leg geometry



Source: Orea et al., 2019.

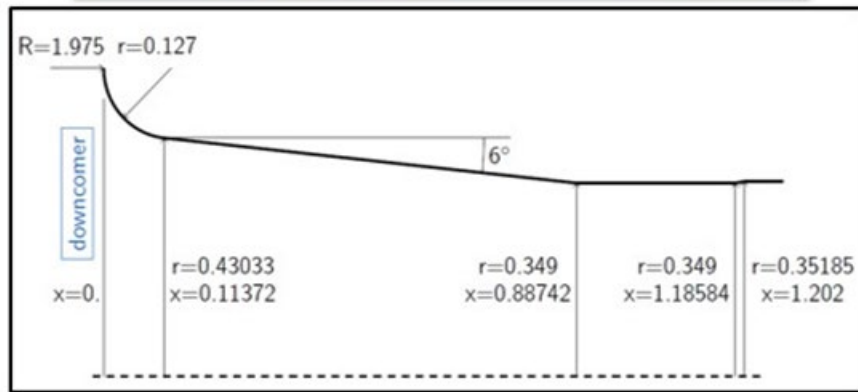
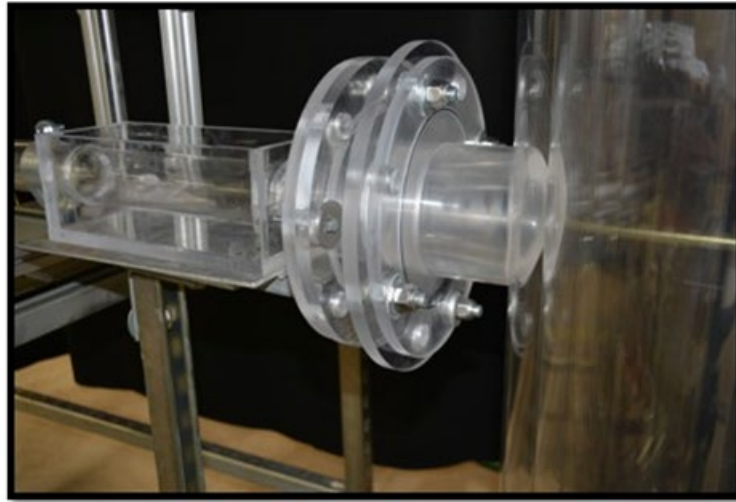
Table 3.1. Dimensions of vessels and cold leg

	Symbol	Description	Dimension (cm)
Heavy Side Vessel	ID <sub>HV</sub>	Inner Diameter of Heavy Vessel	34.29
	H <sub>LC-HB</sub>	Leg Centerline to Bottom of Heavy Vessel	10.9
Cold Leg	ID <sub>LC-HB</sub>	Inner Diameter of Cold Leg	5.31
	L <sub>L</sub>	Total Length	130.81
	L <sub>LL</sub>	Length of Left Section	39.37
	L <sub>LR</sub>	Length of Right Section	91.44
	D <sub>PT</sub>	Distance of Pressure Taps from Valve Midplane	15.98
Light Side Vessel	ID <sub>LV</sub>	Inner Diameter of Outer Cylinder (Vessel)	34.29
	OD <sub>LV</sub>	Outer Diameter of Inner Cylinder (Barrel)	30.48
	H <sub>LC-LB</sub>	Cold Leg Centerline to Bottom Plate	80.33
	H <sub>L</sub>	Cold Leg Centerline to Top Lid	27.94

Source: Orea et al., 2019.

It was proposed to implement a reactor-like geometry of the cold leg and downcomer junction using a conical shape and a rounded edge. The top image of Figure 3.3 shows the nozzle sitting flush against the vessel wall, while the bottom image shows the nozzle dimensions required to achieve the best possible fit.

Figure 3.3. Cold leg vessel nozzle



Source: Orea et al., 2019.

## 4. Test conditions and measurement locations

Two tests (identified as open test [OT] and blind test [BT]) were conducted under different test conditions. The OT was executed using two solutions with a target density difference of  $100 \text{ kg/m}^3$ . The BT was executed using two solutions with a target density difference of  $200 \text{ kg/m}^3$ .

### Fluid properties

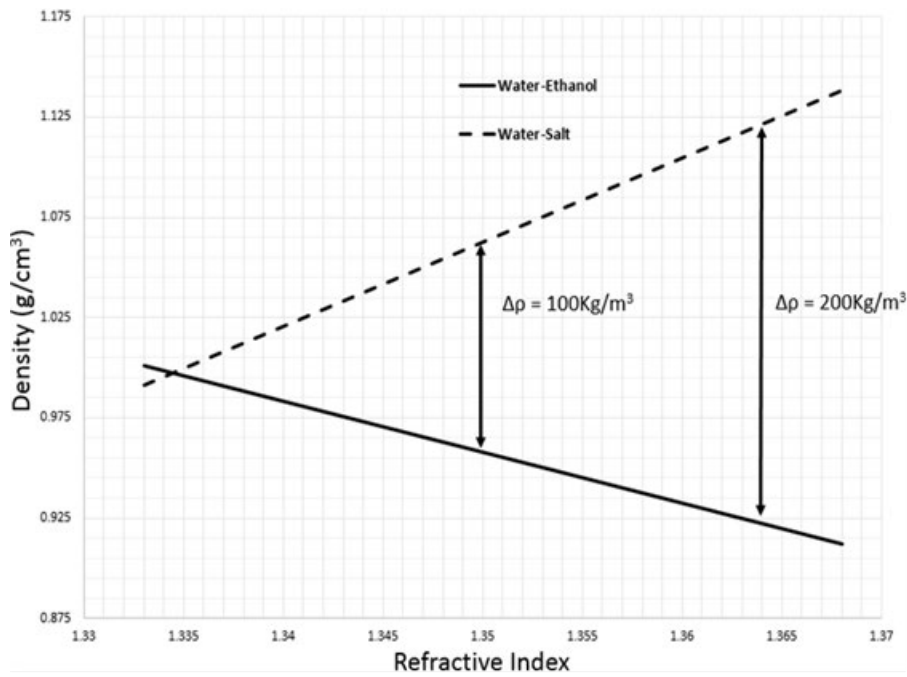
To confirm that the refractive index remained constant during mixing of the selected solutions, the refractive index of a solution generated by the mixing of the two surrogates at different ratios was measured. Density, viscosity, and index of refraction of the parent solutions and intermediate mixtures were measured and reported in s. One can observe that the index of refraction is stable while the two solutions mix. This condition is important when applying the flow visualisation and measurements techniques. Densities were calculated by measuring the weight of a 10 ml sample taken from a batch of solution maintained at a given temperature. The 10 ml volume is extracted using an electronic pipette. The weight of the sample taken is measured with an analytical balance accuracy. The sample is transferred to a glass beaker and placed on the plate of scale. Measurements were performed on solutions in thermal equilibrium with the laboratory environment temperature at an average of  $21^\circ\text{C}$ . Viscosity was measured using a cylindrical system coupled with a double-couette to increase the surface area, yielding enhanced accuracy. The accuracy the instrumentation can be found in Table 4.1. Viscosity was measured at an ambient temperature of  $20.5^\circ\text{C}$ . Figure 4.1 shows the calculated densities of the surrogate fluids and the associated refractive index. Figure 4.2 presents the viscosity of the mixtures for both OT and BT. It can be seen that viscosity is a linear function of the mixture density. This function is displayed in the figure.

**Table 4.1. Fluid properties of sampled mixtures (OT)**

Fluid Properties of Sample Mixtures (Ethanol-Water : Salt-Water ) %*volumetric									
Sample	1	2	3	4	5	6	7	8	9
Ratio	100:0	87.5:12.5	75:25	62.5:37.5	50:50	37.5:62.5	25:75	12.5:87.5	0:100
Density (g/cm <sup>3</sup> )	0.95963	0.97057	0.9866	0.9975	1.00827	1.02575	1.03839	1.05235	1.0649
Viscosity (Pa·s)	0.002334	0.002182	0.002038	0.001875	0.001737	0.00155	0.001459	0.001282	0.001181
Refractive Index	1.3515	1.3505	1.3515	1.3513	1.3509	1.3510	1.3507	1.3510	1.3505

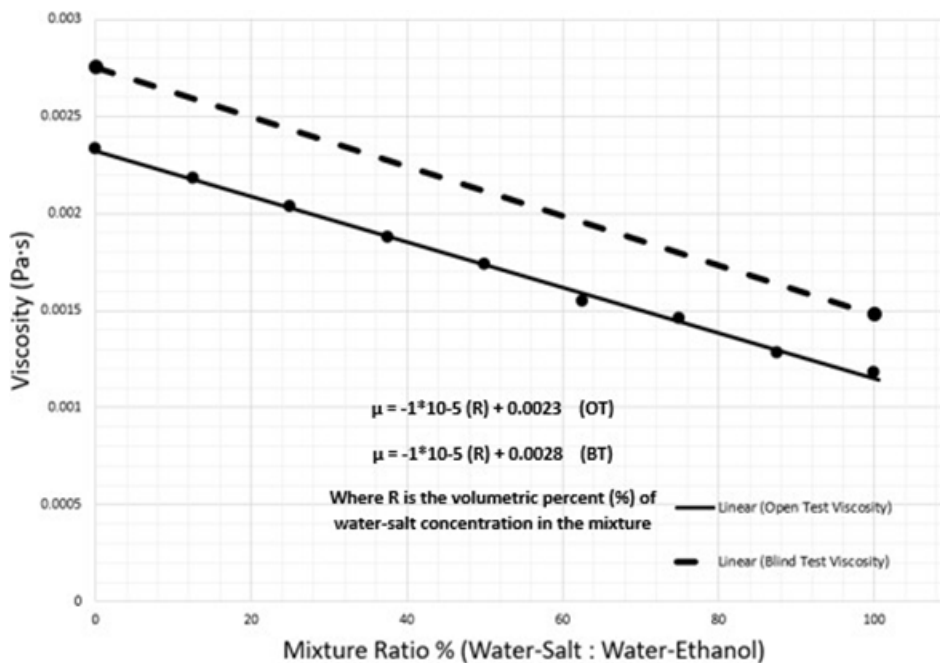
Source: Orea et al., 2019.

Figure 4.1. Density vs. refractive index of solutions



Source: Orea et al., 2019.

Figure 4.2. Viscosity of fluid mixtures



Source: Orea et al., 2019.

All tests were performed with both solutions at a constant ambient temperature of  $21^\circ\text{C} \pm 0.3$ . Figure 4.2 shows the liquid level labelled as Height of Heavy fluid (HH) and the Height of Light vessel labelled (HL). The OT and BT targeted test conditions were

discussed during the benchmark definition and are summarised in Table 4.2. The height of the heavy fluid is calculated from the densities of the surrogate solutions in order to equalise the pressure at the centreline across the isolation valve at the start of the test.

$$H_H = \frac{\rho_L}{\rho_H} H_L$$

Where  $H_L$  is fixed at 27.9 cm.

**Table 4.2. OT and BT fluid properties**

	OT				BT			
	Density (kg/m <sup>3</sup> )	Viscosity (Pa-s)	Solution Concentration (Mass %)	H <sub>H</sub> (cm)	Density (kg/m <sup>3</sup> )	Viscosity (Pa-s)	Solution Concentration (Mass %)	H <sub>H</sub> (cm)
<b>Heavy Fluid</b>	1064.7	0.00109	9.5% salt mass	25.06	1110.7	0.001485	16.0% salt mass	22.99
<b>Light Fluid</b>	956.54	0.00245	26.0% ethanol mass		915.27	0.002755	46.0% ethanol mass	

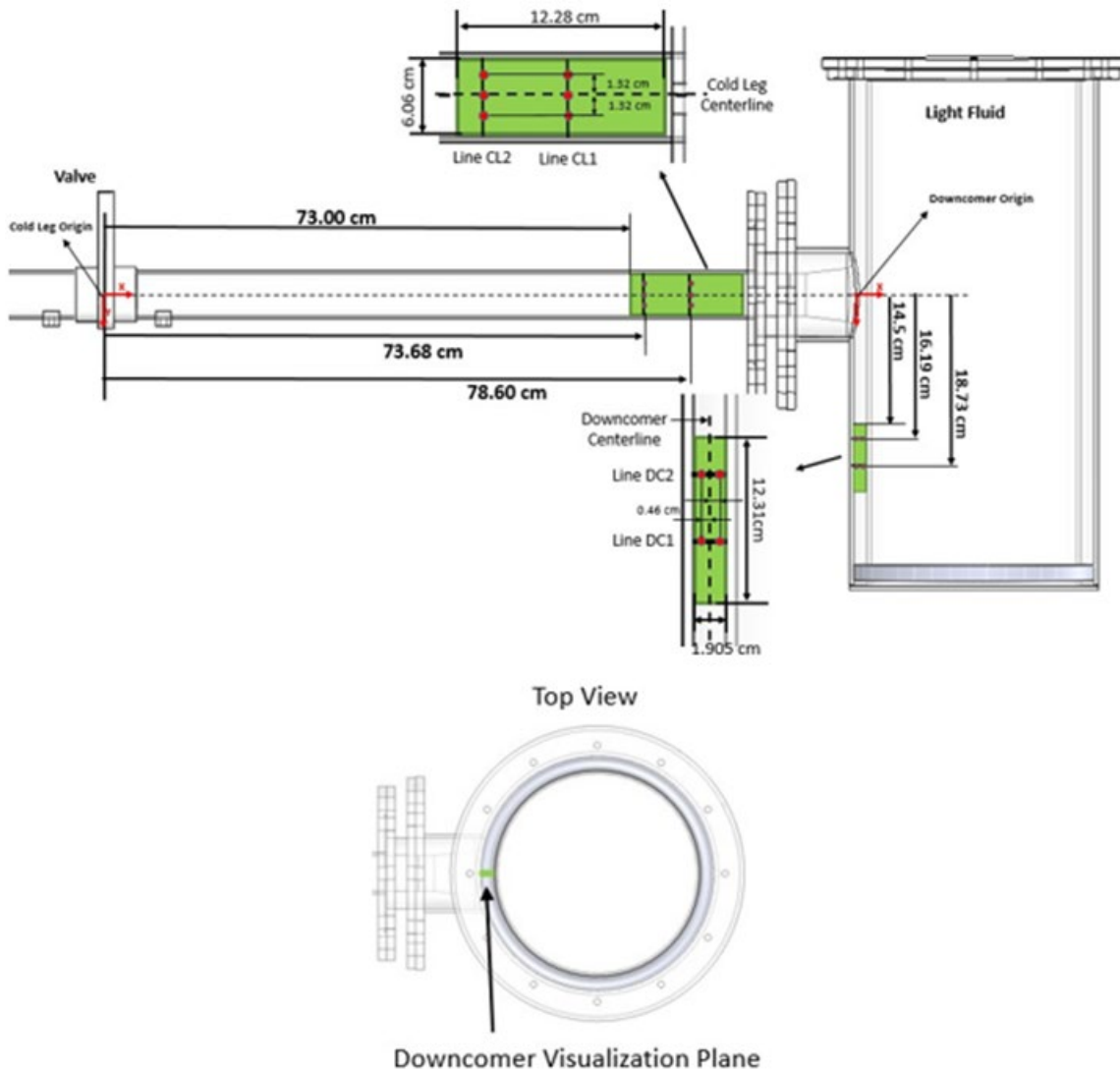
Source: Orea et al., 2019.

Note: These boundary conditions were the ones measured at the test start and are within the uncertainty of the boundary conditions measured during the benchmark definition.

## Measurement locations

The location and dimensions of the two measurement/visualisation windows, together with the reference co-ordinate systems are shown in figure 4.3. The two windows are symmetric across their individual axes.

Figure 4.3. Visualisation windows relative to the valve centreline



Source: Orea et al., 2019.

In addition to the velocity and concentration, the pressure difference was measured across the isolation valve and recorded for the duration of the experiment. Figure 4.2 shows the location of the pressure taps.

## 5. Experimental methods and measurement techniques

The experimental facility is designed to simulate the buoyancy-driven flow between cold and hot water typical of cold water injection events taking place in the cold leg and the downcomer. The facility produces high-fidelity experimental data in a prototypical geometry to test uncertainty quantification methods in conditions closer to real reactor applications. To simulate the mixing phenomena of hot and cold water but also maintain low operating pressures and temperatures for practical reasons, two surrogate solutions of different densities were carefully chosen and prepared to represent the cold and hot fluids. The cold fluid is simulated using a solution of water and salt. A solution of water and ethanol was used to simulate the hot fluid. Concentrations of salt and ethanol in water were selected to achieve the desired density difference between the heavy and light solutions. The properties of the solutions (density, viscosity and index of refraction) were measured and recorded before the test.

Local variations in the refractive index (RI) in the flow cause potential issues when attempting to apply optical measurement techniques such as PIV and laser induced fluorescence (LIF). This issue can be resolved by RI matching. It was possible to find surrogate solutions of specific concentrations that at a given density difference will result in matching refractive indexes. As discussed in the introduction, previous tests identified a combination of ethanol and sodium chloride (NaCl) to be the most suitable for experiments of a larger scale and it was therefore also chosen for this study. High resolution measurements of velocity and concentration fields were performed using specialised laser-based techniques.

### Particle image velocimetry

PIV is a non-intrusive, laser-based optical measurement technique to quantify the velocity vector fields of a fluid. The displacement of fluid elements is captured by using highly reflective, low density micro seeding particles that follow the fluid flow without impacting the flow characteristics. A laser sheet is used to illuminate the test section and particles. A series of images are captured using a high resolution camera at a desired frequency. Images captured are processed using in-house codes and a velocity vector field is constructed. These tracer particles scattered the laser light back to the PIV cameras as they passed through the laser sheets at the regions of interest.

Velocity vectors were retrieved by processing image pairs using PIV analysis software (PRANA) (Nguyen et al., 2017; Eckstein and Vlachos, 2009). All PIV images captured by the 12-bit depth cameras were processed by the advance multi-pass, multi-grid PIV processing algorithms based on the robust phase correlation (RPC) algorithms implemented in the PRANA codes by Virginia Tech. A three-step processing was applied. The initial interrogation window was a 64x64 pixel area, followed by two interrogation areas of 32x32 pixels. All passes had a 50% window overlap. Velocity vectors were calculated from the correlation map with a Gaussian peak fit for sub-pixel accuracy (Raffel et al., 2007). Each pass contained statistical validation of erroneous vectors. A median filter (Westerweel, 1994) was applied, standard deviations of the neighbouring vectors were used to filter out spurious vectors, and blanks were filled by velocity interpolation.

The PIV measurement areas had 37x80 instantaneous velocity vectors in the cold leg region and 20X80 instantaneous velocity vectors in the downcomer region. The spacing of adjacent vectors at the cold leg was 0.155 cm. The spacing of the adjacent vectors at the downcomer was 0.105 cm.

### Laser induced fluorescence

LIF is a laser-based measurement technique used to measure the temperature or concentration of fluids. A soluble tracer dye is uniformly mixed with the fluid. A laser sheet illuminates the test section, causing the particles to fluoresce. A series of images are captured using a high resolution camera. Concentration distributions can be constructed by converting the camera signal intensity into physical concentration from the images captured and processed using in-house codes. For this experiment, Rhodamine 6G (absorption peak at 532 nm and emission peak at 552 nm) was used as the tracer dye. This fluorescent dye was selected due to its negligible response to temperature changes, which makes it suitable for concentration measurements.

### LIF calibration

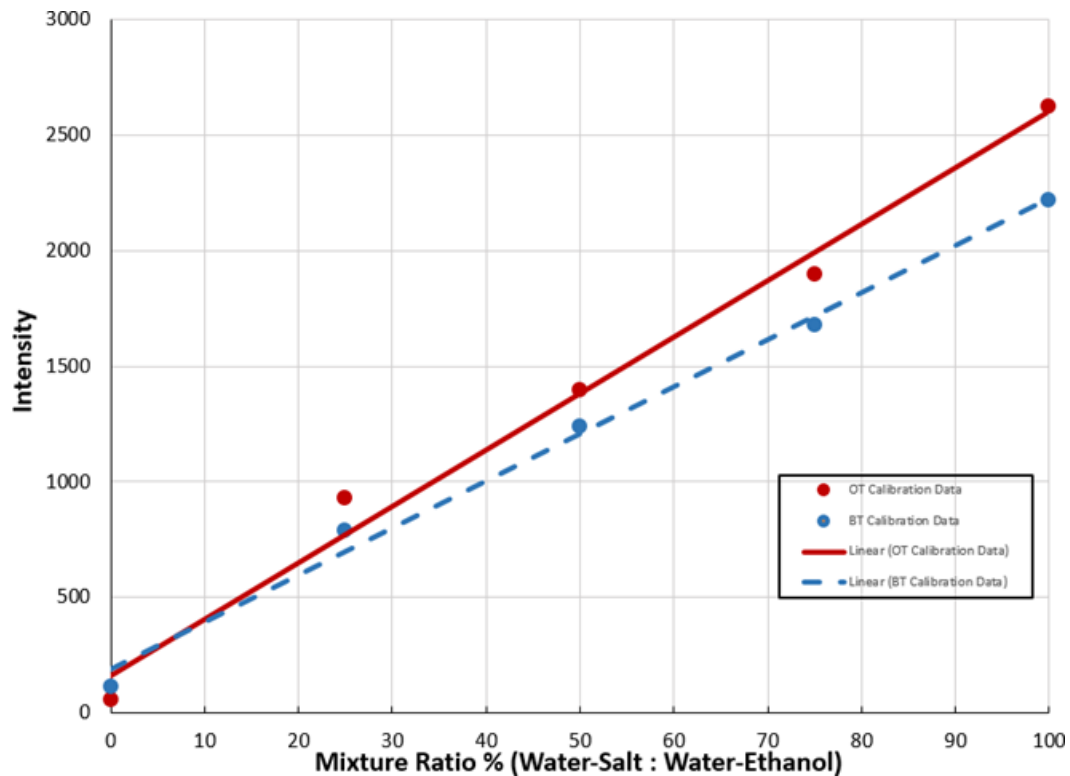
The intensity of the light emitted by the dye was correlated to the concentration of the solutions by performing a five-point in situ calibration. Rhodamine 6G was dissolved to a parent heavy solution with the same concentration used during the test. From this parent solution (100% heavy solution calibration point), three additional solutions were prepared by mixing it with an amount of light solutions. These solutions were used for the 75%, 50%, and 25% calibration points. One additional point was included to account for pure light solutions (0% calibration point). To apply the best possible calibration to the captured images, two calibration methods were attempted.

The first method involved using a single mean intensity value from a captured imaged for each calibration point. The average intensity is calculated by summing each pixel intensity and dividing by the total number of number of pixels.

$$I_{avg} = \frac{1}{N} \sum_{p=1}^N I_p$$

Where  $I$  is the signal intensity,  $N$  is the total number of pixels, and  $p$  is the pixel index. By calculating the mean intensity for five known concentrations, a linear curve can be estimated to then apply to the open test and blind test. These plots can be seen in Figure 5.1 for the open test and blind test calibrations.

Figure 4.1. OT and BT LIF 5-point calibration curve from window average intensity



Source: Orea et al., 2019.

On the plots, the slope represents the increasing intensity as the mixture ratio approaches 100% water-salt. The result is a linear expression for calculating the concentration.

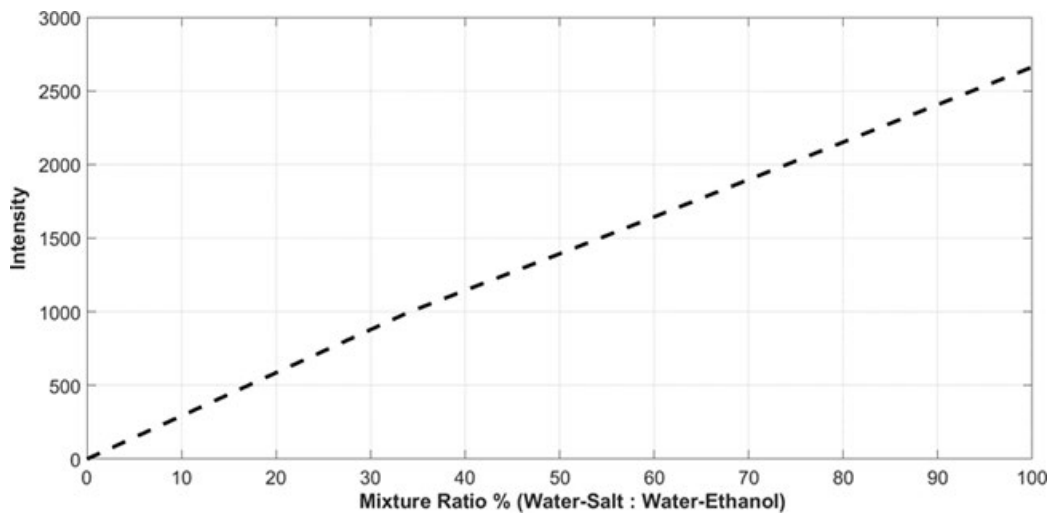
$$C_{OT} = 0.0409 * I(i, j) - 6.484$$

$$C_{BT} = 0.0489 * I(i, j) - 9.138$$

The second method involved a local pixel intensity averaging from each calibration point. An 8 by 8-pixel area is averaged for the entire image size. This was applied to five known concentrations. A second-degree polynomial fit was then applied to each co-ordinate for all concentrations from 0-100% mixture ratio.

$$C(X, Y) = A(X, Y) * I(i, j)^2 + B(X, Y) * I(i, j) + C(X, Y)$$

Where C is the concentration at the point, I is the intensity at the point, i and j are pixel indexes, and A, B, C are a two-dimensional coefficient matrices created by curve fitting. This process was repeated for open tests and blind tests. An example of the polynomial fit at the centre point of an image with varying intensities is shown in Figure 4.2.

**Figure 4.2. OT LIF 5-point local calibration curve for a single point in point in space**

Source: Orea et al., 2019.

Based on the calibration methods applied, the second polynomial curve was used to calculate fluid concentrations.

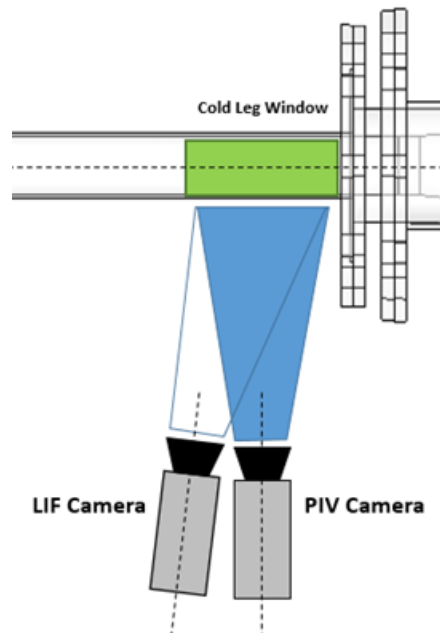
## Experimental method

PIV and LIF techniques were used to capture the concurrent velocity and concentration fields in the cold leg region and PIV was used to capture the velocity vector field in the downcomer region (Díaz, Castanedo and Palomar, n.d.; Odier, Chen and Ecke, 2014; Xu and Chen, 2012). The solutions were uniformly seeded with silver-coated hollow glass spheres (mean diameter of 16  $\mu\text{m}$  and a density of 1.6  $\text{g cm}^{-3}$ ) to perform the PIV measurements. The PIV and LIF systems consisted of a laser source with appropriate optics to create two 1-mm laser sheets at the regions of interest (Figure 4.2). Three digital CMOS cameras with a full resolution of 1280 x 800 pixels were used. Two cameras were installed to record PIV and LIF data at the cold leg, and one camera was used to record PIV data at the downcomer. Camera settings were optimised based on the visualisation window and the flow observations performed during shakedown tests (1 280 x 600 resolution at the leg and 1 280 x 320 at the downcomer). Fluorescent dye (Rhodamine 6G) was homogeneously mixed with the heavy solution to perform concentration measurements using LIF. This preparation was completed earlier enough from the test initiation to allow the solutions to reach thermal equilibrium with the laboratory environment. Two thermocouple probes were utilised to monitor and measure the temperature of the heavy and light solutions respectively, before and during the experiments. Pressure across the isolation valve was verified at the beginning of each test and monitored and recorded during the duration of the tests using a high accuracy differential pressure transducer.

With the isolation valve closed, the light solution was transferred into the light vessel to be filled up to the level of the top lid. The heavy solution was then transferred into the heavy vessel up to a level estimated to balance the hydrostatic pressure across the centre line of the isolation valve. Air pockets formed during the fluid transfer were carefully removed before each test. The experiment was initiated by releasing the spring mechanism connected to the isolation valve which lifted the guillotine valve and

triggered the visualisation systems. Camera recording start times and durations were optimised based on the observed arrival and transition times of the heavy fluid front during previous shakedown tests. The LIF camera was set next to the PIV camera at a small angle as seen in Figure 5.3. The frame of the LIF images contained that of the PIV images.

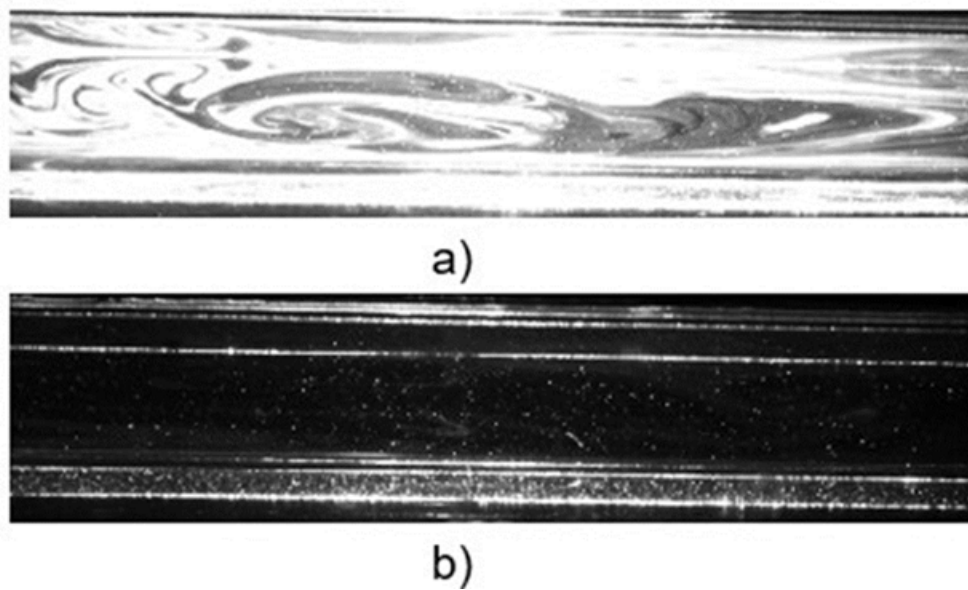
**Figure 5.3. Camera setup for cold leg window**



Source: Orea et al., 2019.

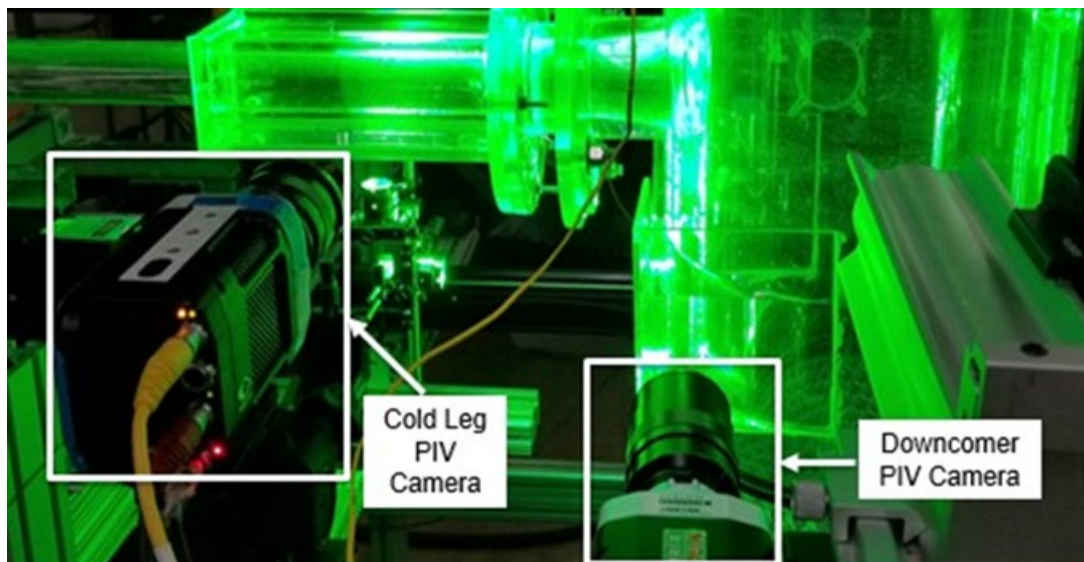
To avoid interference between the two techniques, the LIF camera was fitted with a 590 nm band pass filter that allowed for the Rhodamine-6G emission wavelength to pass and reflected the laser light scattered from the particles. Similarly, the PIV camera was fitted with a 532 nm band pass filter that allowed laser light scattered from the particles to pass but reflected fluorescent light. Figure 5.4 shows two images with and without the appropriate light filters. Figure 5.5 shows the camera system being applied to the cold leg and downcomer for PIV only.

Figure 5.4. Cold leg visualisation and filter effect



Note: a) Image without 552 nm light filter. b) Image with 552 nm light filter.  
Source: Orea et al., 2019.

Figure 5.5. Camera system for simultaneous PIV measurements



Source: Orea et al., 2019.

A full list of the equipment and instrumentation used during experiments can be found in Table 5.1.

Table 5.1. Equipment and instrumentation specification

#	TYPE	MODEL	PURPOSE	ACCURACY	COMMENTS
1	CAMERA	Phantom MIRO M310	Capture Images for LIF in Cold Leg Region	N/A	OT: 250 frames/sec BT: 500 frames/sec
2	CAMERA	Phantom MIRO M310	Capture Images for PIV in Cold Leg Region	N/A	OT: 250 frames/sec BT: 500 frames/sec
3	CAMERA	Phantom MIRO M310	Capture Images for PIV in Downcomer Region	N/A	OT: 250 frames/sec BT: 500 frames/sec
4	Pressure Transducer	OMEGA:MMDWB10W BIV5P2D0T2A2CE	Measure Pressure Drop across Isolation Valve	$\pm 0.361$ PSID (Pressure Range)	
5	Thermocouple	K Type	Measure temperature at bottom of heavy water tank	Standard: $\pm 2.2$ C or $\pm 0.75\%$	Temperature was measured to be $20.5 \pm 0.3$ °C
6	Thermocouple	K Type	Measure temperature at top of light water annulus	Standard: $\pm 2.2$ C or $\pm 0.75\%$	Temperature was measured to be $20.5 \pm 0.3$ °C
7	DAQ	NI SCXI-1303	Collect pressure/temperature Data		1000Hz sampling rate
8	Laser	CHANGCHUN NEW INDUSTRIES MGL-W-532 20W	Create LIF/PIV Laser Sheet		Continuous Laser
9	Mass Scale	Mettler Toledo AB analytical balance (Model. AB204-S)	Measure mass of samples	$\pm 0.0001$ g	
10	Pipette	Eppendorf Repeater Xstream	Measure fluid volume	$\pm 0.055$ ml	
11	Rheometer	MCR 300 Modular Compact Rheometer	Measure viscosity of working fluids	$\pm 0.5\%$	Viscosity is measured at $22.4$ °C
12	Refractometer		Measure Refractive Index	$\pm 0.0005$	RI is measured at $22.4$ °C
13	LaVision Filter	LIF camera Filter for CL region	Filter light coming from PIV particles	BP590nm-67FWHM	
14	Edmund Filter	PIV camera Filter for CL region	Filter light coming from LIF dye	BP532nm-10FWHM	

Source: Orea et al., 2019.

## 6. Uncertainty analysis

### *PIV uncertainty*

PIV uncertainty analysis employs the method applied in (Sciacchitano, 2019). Calculated velocity can be expressed as,

$$U = \alpha \left( \frac{\Delta X}{\Delta t} \right) + \delta U$$

where  $\Delta X$  is the displacement of particle images,  $\Delta t$  is the time interval of successive images,  $\alpha$  is the magnification factor identified through a calibration, and  $\delta U$  is the uncertainty factor of the flow field. The uncertainty of the measured velocity can be calculated by propagating the uncertainties of alpha, position, time and  $\delta U$ ,

$$\sigma_U = \sqrt{\left( \frac{\Delta X}{\Delta t} \right)^2 \sigma_\alpha^2 + \left( \frac{\alpha}{\Delta t} \right)^2 \sigma_{\Delta X}^2 + \left( \frac{\alpha \Delta X}{\Delta t^2} \right)^2 \sigma_{\Delta t}^2 + \sigma_{\delta U}^2}$$

where,

- $\alpha$ : magnification factor estimated by in situ calibration;
- $\sigma_{\Delta X}$ : displacement uncertainty determined by the performance of the PRANA code;
- $\Delta t$ : time interval uncertainty determined by camera settings;
- $\sigma_{\delta U}$ : uncertainty factors of flow field estimated by particle density and diameter.

The magnification factor  $\alpha$  is estimated by in situ calibration. The conversion from pixels to millimeters was performed by taking calibration images of targets with known physical dimensions. Images captured during calibration gave correlated pixels to a physical distance of  $\alpha_{CL} = 0.0962$  mm/pix for the cold leg OT and BT. Downcomer calibration images gave  $\alpha_{DC} = 0.0655$  mm/pix for OT and BT. Image and lens distortions create slightly varying magnification factors. This results in  $\sigma_{\alpha,CL} = 0.000617$  mm/pix and  $\sigma_{\alpha,DC} = 0.000276$  mm/pix for the for OT and BT, respectively.

The uncertainty from the vectors calculated is determined by the performance of the PRANA code which has been thoroughly studied (Timmins et al., 2012; Wilson and Smith, 2013). These studies have reported an overall  $\sigma_{\Delta X}$  uncertainty of approximately 0.1 pixels. The spurious and erroneous vectors were evaluated for all time-resolved PIV velocity vectors. For all tests, OT and BT, less than 1.5% of vectors were erroneous.

**Table 6.1. Values used for OT and BT uncertainty analysis**

	<b>Cold-Leg</b>	<b>Downcomer</b>
<b><math>\alpha</math> (mm/pix)</b>	0.0962	0.0655
<b><math>\sigma_\alpha</math> (mm/pix)</b>	0.000617	0.000276
<b><math>\sigma_{\Delta x}</math> (pix)</b>	0.1	0.1

Source: Orea et al., 2019.

The time interval between frames recorded by the high-speed camera used during the experiment is  $\Delta t$ . The cameras recorded images at a rate of:  $f_{OT} = 250$  Hz and  $f_{BT} = 500$  Hz. Subsequently,  $\Delta t_{OT} = 0.004$  s and  $\Delta t_{BT} = 0.002$  s. The uncertainty given by the camera settings is 1% which corresponds to  $\sigma_{t,OT} = 0.04$  ms and  $\sigma_{t,BT} = 0.02$  ms.

The value  $\sigma_{\delta U}$  can be considered negligible as it describes the behaviour of the particles in the fluid. As mentioned in the section describing the PIV methodology, the particle's diameter and density are sufficiently small and low to properly follow the fluid flow.

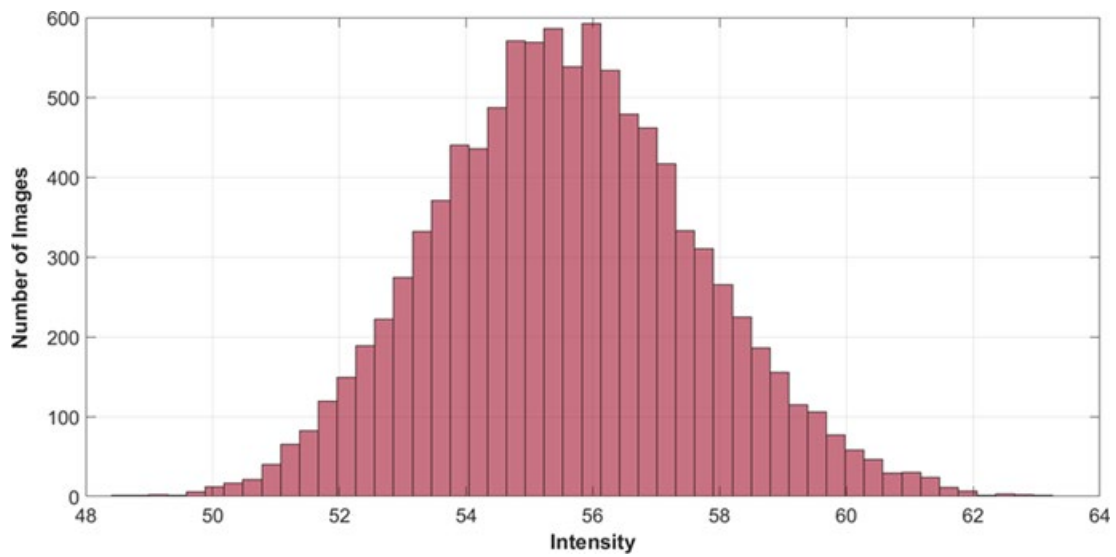
Overall, uncertainty analysis for the OT and BT was performed assuming the maximum amount of error. Note that the same approach is taken for the vertical V components, and uncertainties can be calculated. The maximum errors for PIV measurements for OT and BT were calculated to be,

$$\sigma_{U_{CL,max}} = 0.0027 \text{ m/s}$$

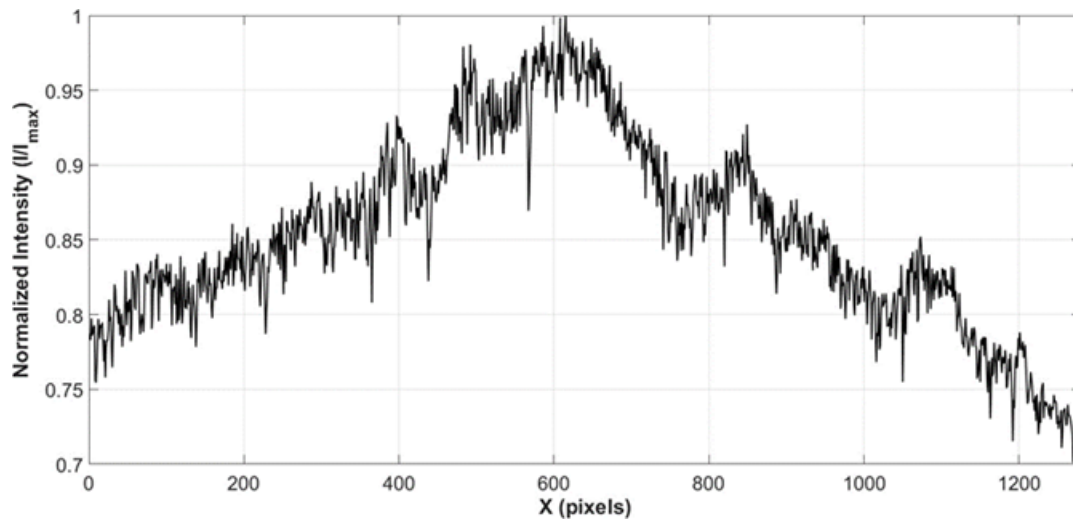
$$\sigma_{U_{DC,max}} = 0.0031 \text{ m/s}$$

### *LIF error sources*

LIF uncertainties are less commonly studied as they are difficult to quantify. In this case, an in situ calibration was performed using five points as previously discussed in the methodology section. After thorough investigation, it was observed that one of the main contributors to error in the LIF data was the volume of dye homogeneously mixed during calibration. Systematic errors that affect to LIF measurements include background light, laser power fluctuations, spatial variation of light intensity, and camera sensor saturation. In order to measure qualitatively the background and laser light, 10 000 images were taken of the facility without any fluorescent dye. Figure 6.1 shows recorded background intensities were small. This error can be eliminated by subtracting background images.

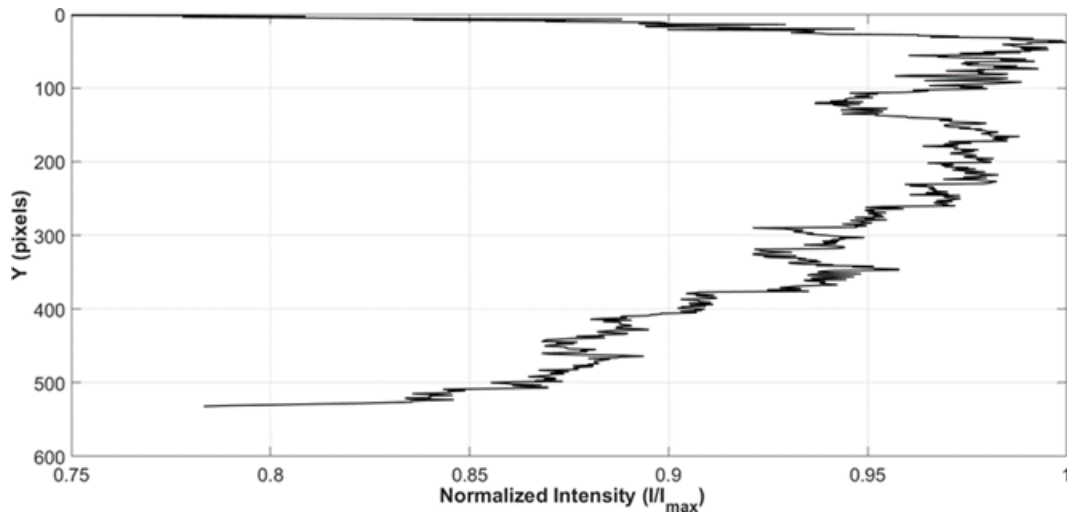
**Figure 6.1. Background intensity distribution**

The laser power distribution also contributes to measurement error as damaged optical lenses and/or a fluctuating lasers will create irregularities in the laser sheet. In addition, small scratches on wall surfaces, micro-bubble formation, and debris will obstruct the laser sheet and cast shadows in the test section. Figure 6.2 and Figure 6.3 demonstrate the effects of laser power fluctuations and spatial distributions on captured images.

**Figure 6.2. Normalised intensity along horizontal profile**

As seen in Figure 6.2, the laser light intensity reaches a maximum near the centre of the frame, and tails off as it moves towards the edges of the frame.

Figure 6.3. Normalised intensity along vertical profile



The laser spatial distribution is also affected in the vertical direction as shown in Figure 6.3. Laser light entering from the top of the visualisation window will be attenuated and decrease in intensity as it traverses the plane. The camera sensor saturation was tested by increasing the concentration of Rhodamine-6G in small increments. To avoid saturating the camera sensor, the amount of Rhodamine-6G injected was set at approximately 65% of the maximum allowed before complete saturation.

The error sources posed a challenge when attempting to quantify into a factor. Therefore, all experiments were performed in situ. In addition, local calibration aided in minimising these effects. By knowing the target concentration during the calibration and the calculated concentration based on a local point-by-point method, the relative error can be calculated with the following expression (Gavelli and Kiger, 1998).

$$\epsilon = \frac{|C_o - C_p|}{C_o} * 100$$

Where  $C_o$  is the known concentration, and  $C_p$  is the calculated concentration using the local method. Applying this to a sample set of 5 000 images of a known 50% water-salt calibration produced an average relative error of OT = 3.64 % and BT = 4.62 %.

Additional information on the experimental test facility, test methods, and uncertainty quantification is available in (Orea et al., 2019).

## 7. Participants and submitted results

Table 7.1 shows the list of participants that submitted simulation results to the benchmark organisers. The table includes a generic description of the computational tools (CFD software), methods adopted and nodalisation of the geometry, and specifies whether uncertainty quantification was conducted.

The different acronyms refer to the following models for turbulent tensor resolution:

- LES: Large Eddy Simulation (high fidelity, direct resolution of large scale of motion, only small scales are modelled, high computational cost, unsteady simulation);
- RANS: Reynolds Averaged Navier-Stokes simulation (industrial use, modelling of the entire flow field, low computational cost, steady state simulation);
- URANS: Unsteady RANS simulation (same as above, unsteady simulation).

Note that time dependent instabilities captured by LES and URANS are different. The resolved flow field from LES takes into account the actual turbulent fluctuations (random). The one from URANS does not contain such information, being representative of coherent fluctuation (periodic) only. Please also note that some LES computations have been made with relatively low nodalisation, similar to other RANS or URANS computations.

Table 7.1. Submitted simulation results

Country	Institution	Name	CFD Software (StarCCM+, CFX, Fluent, etc)	Version (V13, etc)	Method (RANS, URANS, LES...)	Number of nodes	Uncertainty (Yes/No)
France	CEA	Pierre-Emmanuel Angeli	TrioCFD	1.7.8	LES	3,589,347	No
France	EDF	CAMY R., LE COUPANEK E.	Code_Saturne	6.0 alpha	LES	128 M	Yes
France	IRSN	Daniele Vivaldi, Marc Forestier, Jean Baccou	CFX	18.2	URANS	4.3 M	no
France	IRSN	Duval	CALIF <sub>3</sub> -p <sup>2</sup> -REMICS	V1.4	RANS - k-w SST	2,948,188	No
Japan	Japan Atomic Energy Agency	Satoshi ABE	OpenFOAM	2.3.1	LES	8.4 M	Yes
Korea	Seoultech/KAERI	Jungwoo Kim	CUPID	-	RANS	about 0.2M	No
Russia	OKBM	Sveshnikov	CFX	V16.2	LES	11.4 M	Yes
Russia	OKB "GIDROPRESS"	L. Golbrodov, A. Skibin, A. Krutikov, V. Volkov, O. Kudryavtsev, Yu. Nadinskiy	CFX	18.2	LES	37,367,976	No
Russia	ROSATOM (VNIIEF)	Andrey Deulin	LOGOS	V5	LES	12 M	Yes
Spain	Universitat Politècnica de València	Yago Rivera	ANSYS CFX	19.1	LES	4 M	Yes
Unites States	TAMU	Jonathan Lai	Nek5000	17	LES	0.5 B	no

## 8. Benchmark results

Selected velocities and concentrations at identified locations have been included in the benchmark exercise. These include time-averaged streamwise velocities and concentrations.

**Table 8.1. Time-averaged measured quantities**

Location	Quantity	Time intervals (s)
CL1	U(y)	[5-10], [10-15],[15-22]
	C(y)	
DC1	V(x)	[10.5-15.5], [15.5-20.5], [20.5-25.5],
DC2		[25.5-30.5], [30.5-35.5], [35.5-41.5]

The experimental results are plotted (black curves) with the experimental uncertainty range. The CFD results obtained by all 11 participants are plotted on the same graphs.

Please note that the data presented here are only roughly analysed in the synthesis and conclusion section following their presentation and discussions at the meeting on 26 June 2019. Deeper analysis will be presented in a second report.

### Cold leg results – Streamwise time-averaged velocity component (CL1 Location)

The experimental time-averaged velocity component, U, along the probe line CL1 is plotted and compared with the simulation results for five-second intervals.

**Figure 8.1. Y-position vs. U (cm/s) 5-10 second time-averaged U – CL1**

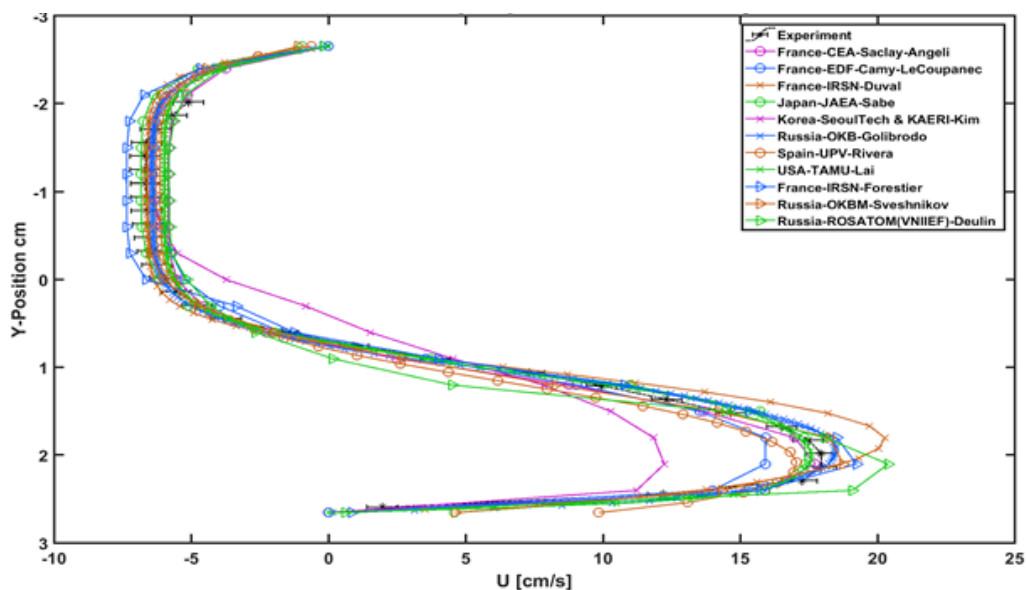


Figure 8.2. Y-position vs. U (cm/s) 10-15 second time-averaged U – CL1

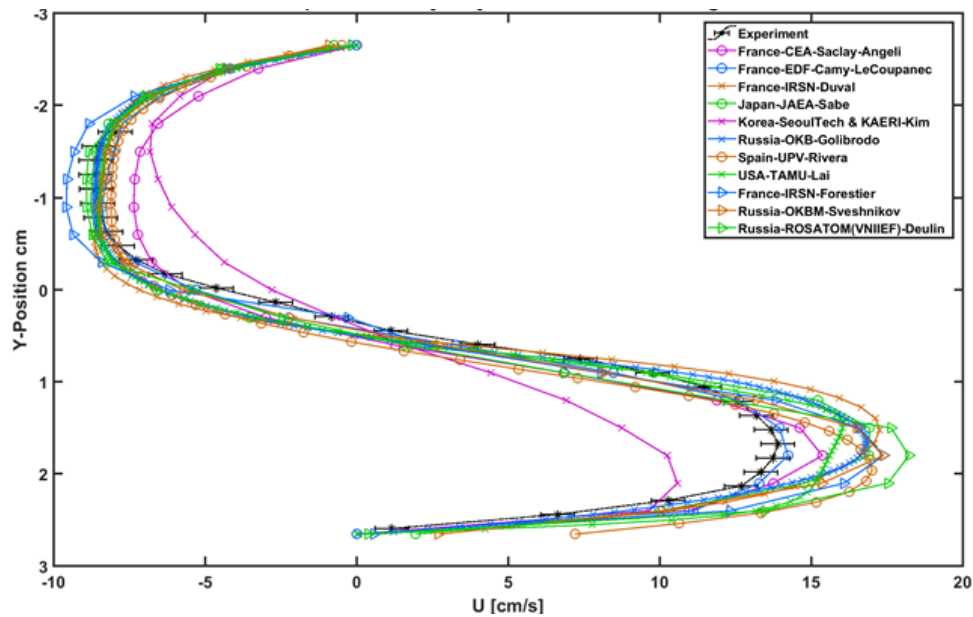
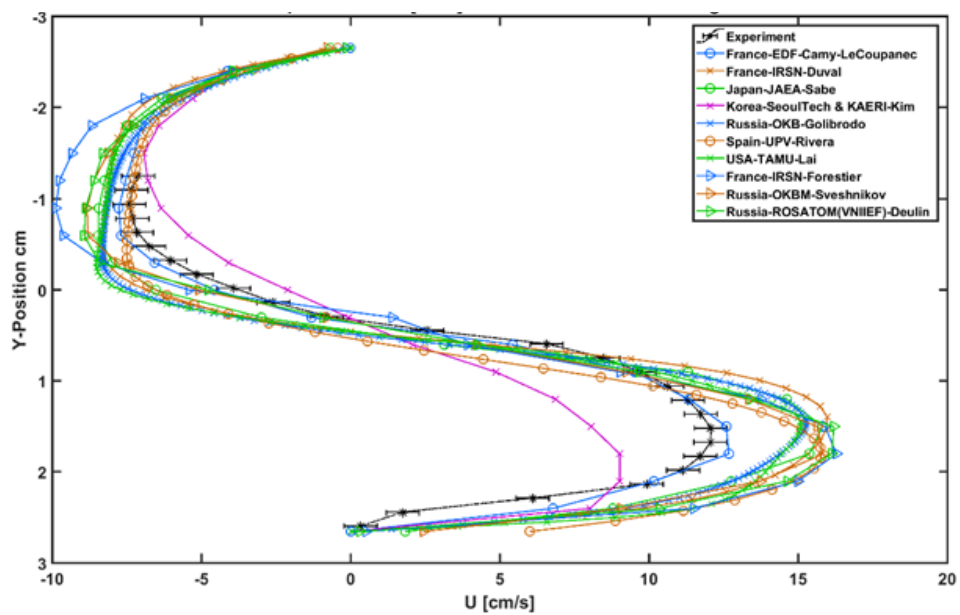


Figure 8.3. Y-position vs. U (cm/s) 15-22.24 second time-averaged U – CL1



### Cold leg results – Time-averaged concentrations

The experimental time-averaged concentration,  $C$  (0% = pure light solution, 100% = pure heavy solution), is plotted and compared with the simulation results for five-second intervals.

Figure 8.4. Y-position vs. concentration (%) 5-10 second time-averaged C – CL1

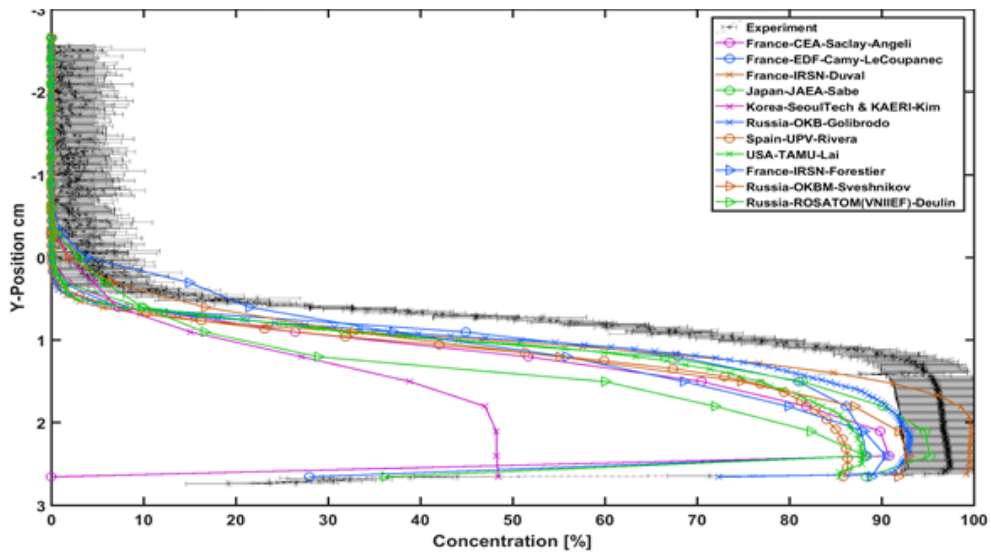


Figure 8.5. Y-position vs. concentration (%) 10-15 second time-averaged C – CL1

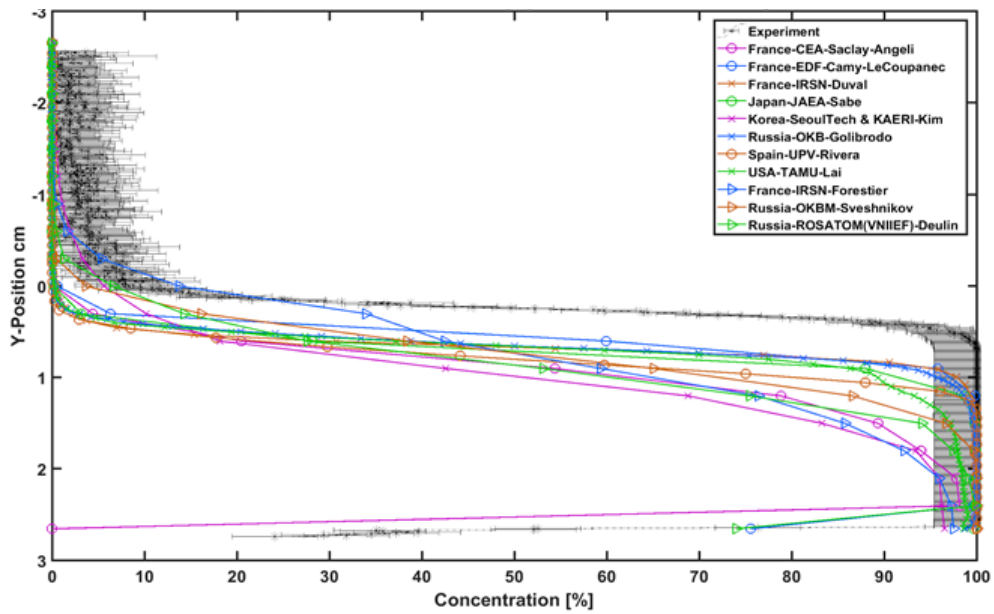
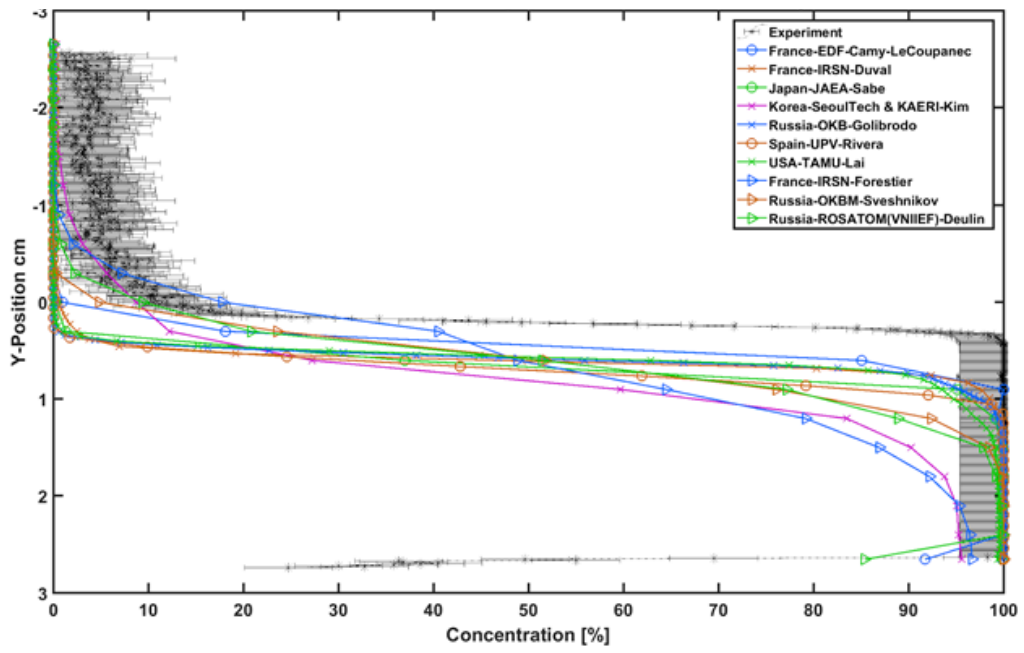


Figure 8.6. Y-position vs. concentration (%) 15-22.24 second time-averaged C – CL1



### Downcomer results – Streamwise time-averaged velocity component (DC1 Location)

The experimental time-averaged velocity component,  $V$ , along the probe line DC1 is plotted and compared with the simulation results for five-second intervals.

Figure 8.7.  $V$  (cm/s) vs. X-position 10.5-15.5 second time-averaged  $V$  – DC1

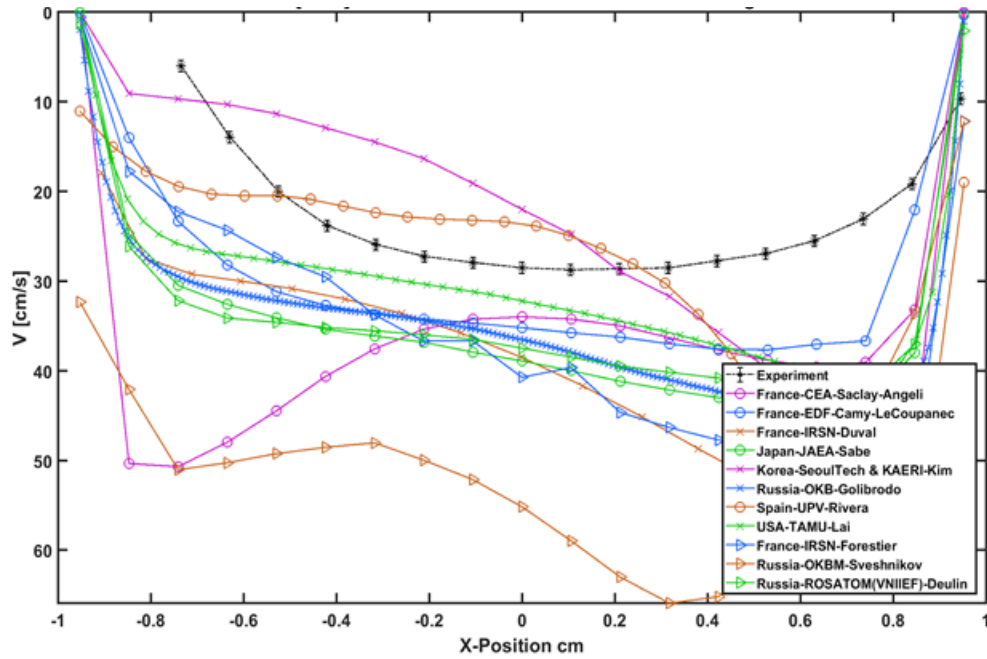


Figure 8.8.  $V$  (cm/s) vs. X-position 15.5-20.5 second time-averaged  $V$  – DC1

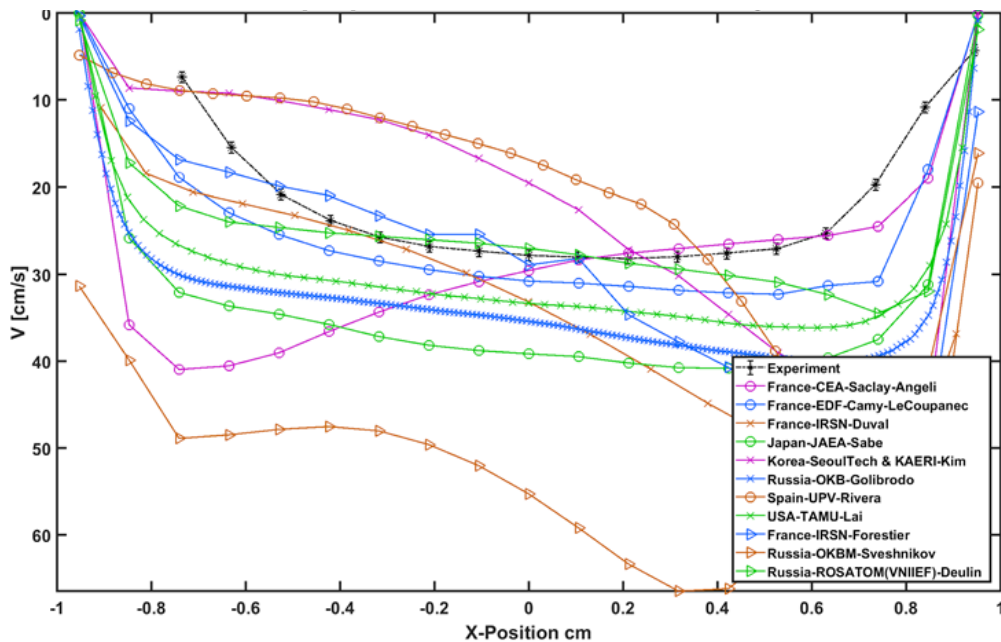


Figure 8.9. V (cm/s) vs. X-position 20.5-25.5 second time-averaged V – DC1

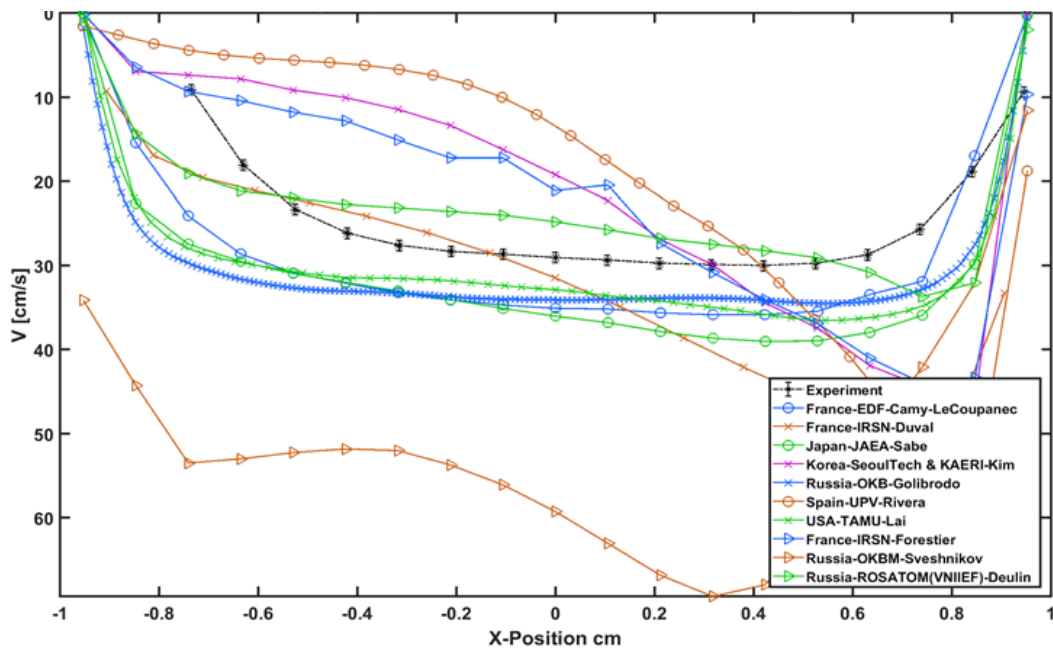


Figure 8.10. V (cm/s) vs. X-position 25.5-30.5 second time-averaged V – DC1

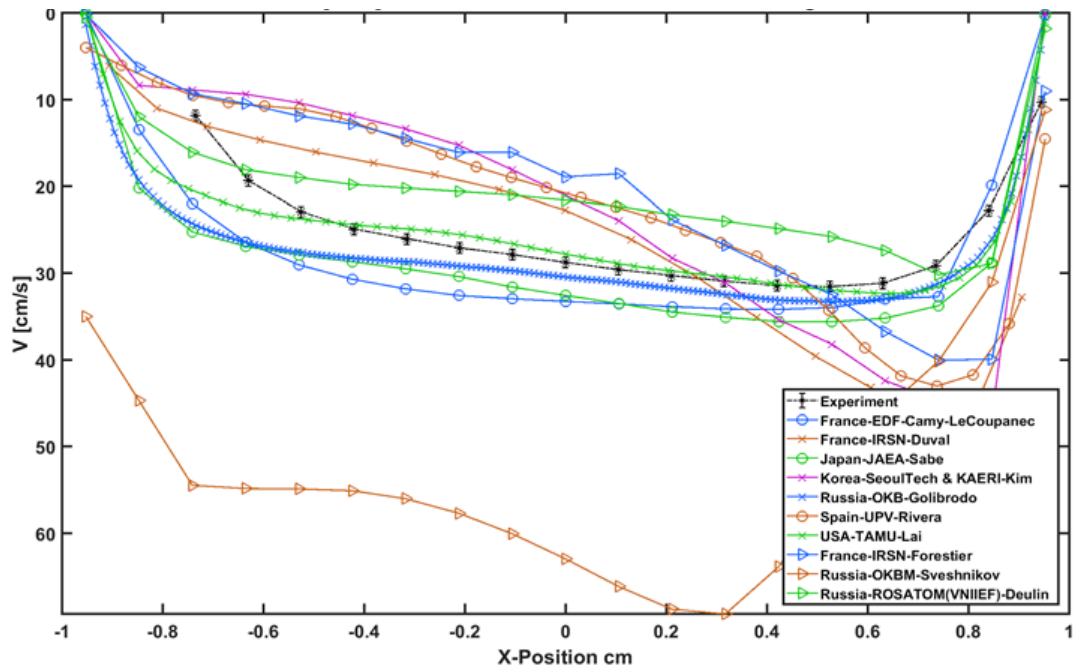


Figure 8.11. V (cm/s) vs. X-position 30.5-35.5 second time-averaged V – DC1

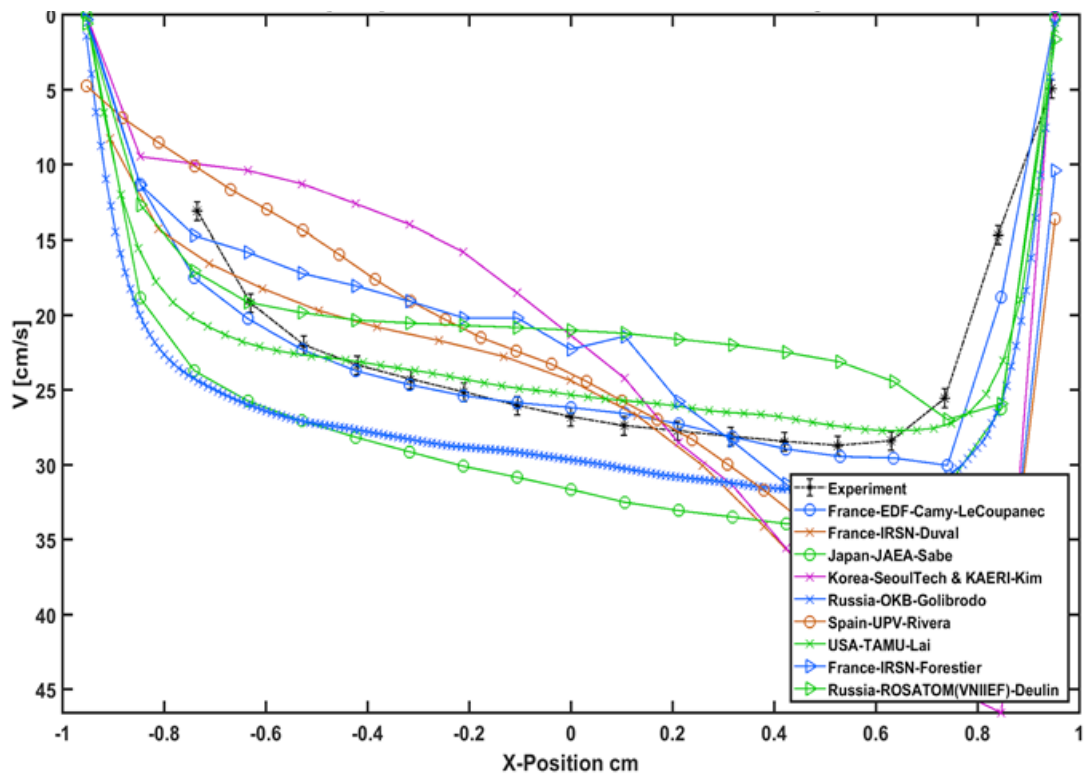
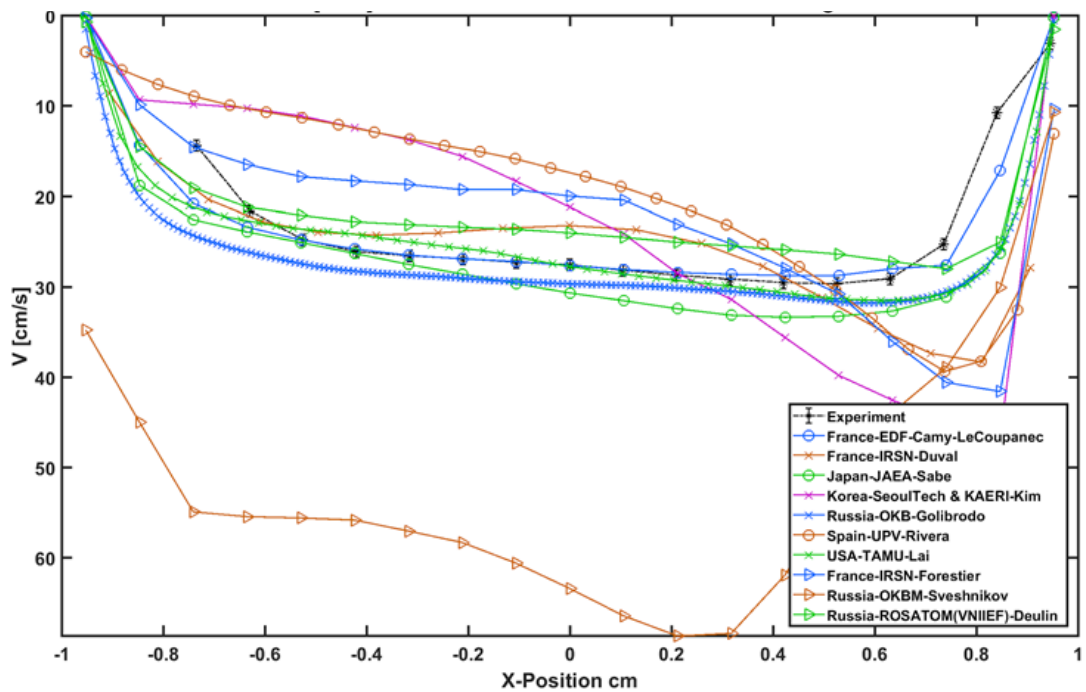


Figure 8.12. V (cm/s) vs. X-position 35.5-41.538 second time-averaged V – DC1



## Downcomer results – Streamwise time-averaged velocity component (DC2 Location)

The experimental time-averaged velocity component,  $V$ , is plotted and compared with the simulation results for five-second intervals.

Figure 8.13.  $V$  (cm/s) vs. X-position 10.5-15.5 second time-averaged  $V$  – DC2

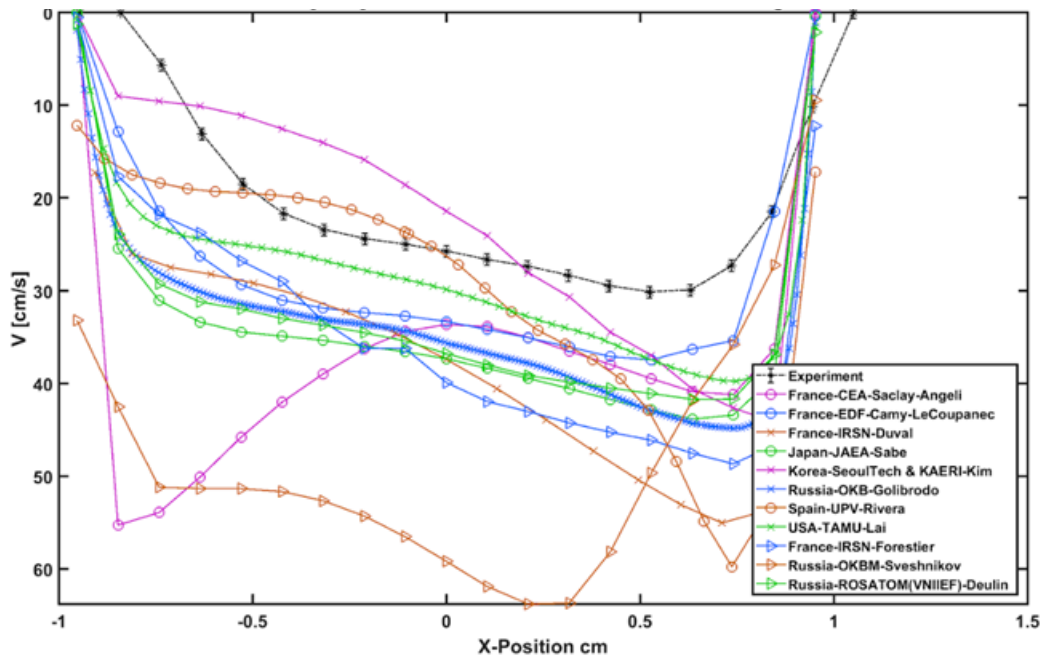


Figure 8.14.  $V$  (cm/s) vs. X-position 15.5-20.5 second time-averaged  $V$  – DC2

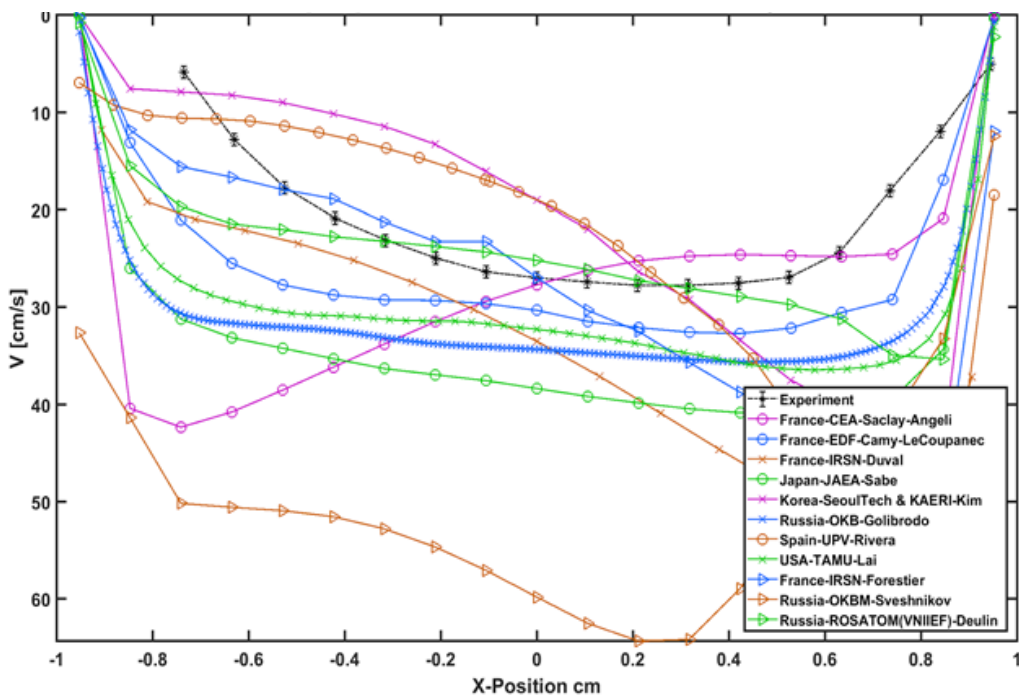


Figure 8.15. V (cm/s) vs. X-position 20.5-25.5 second time-averaged V – DC2

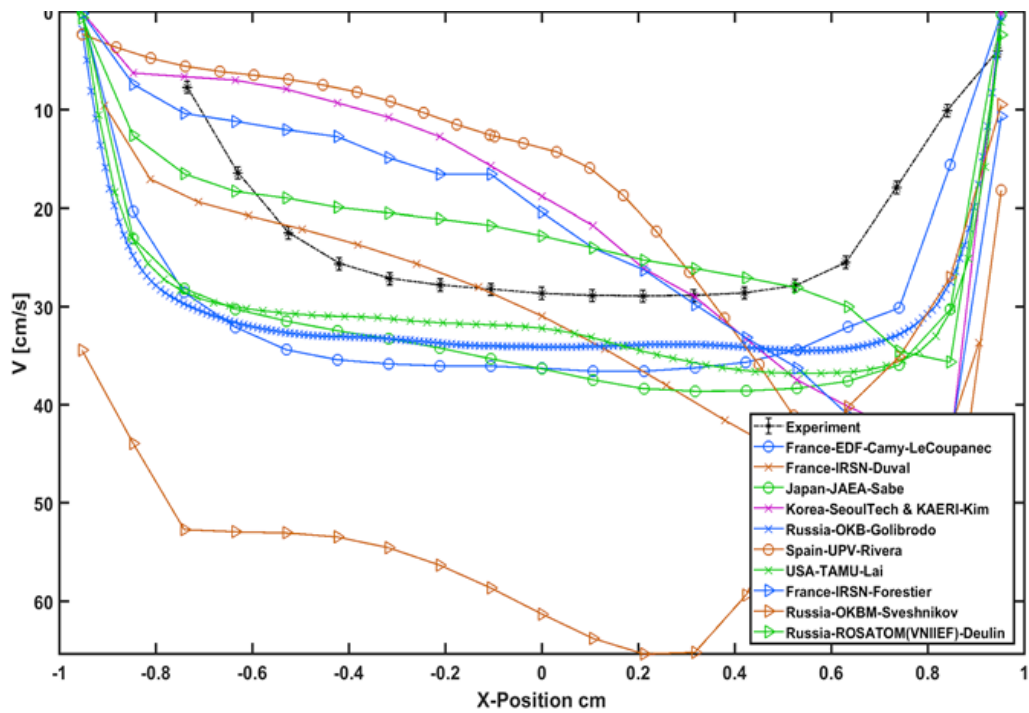


Figure 8.16. V (cm/s) vs. X-position 25.5-30.5 second time-averaged V – DC2

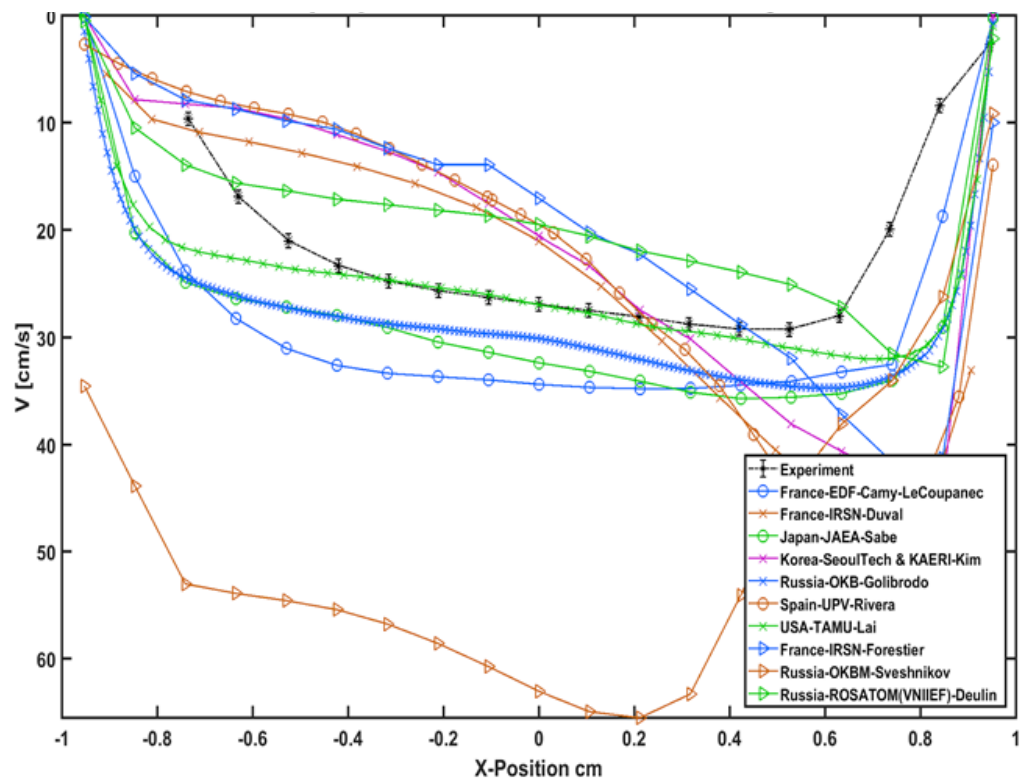


Figure 8.17. V (cm/s) vs. X-position 30.5-35.5 second time-averaged V – DC2

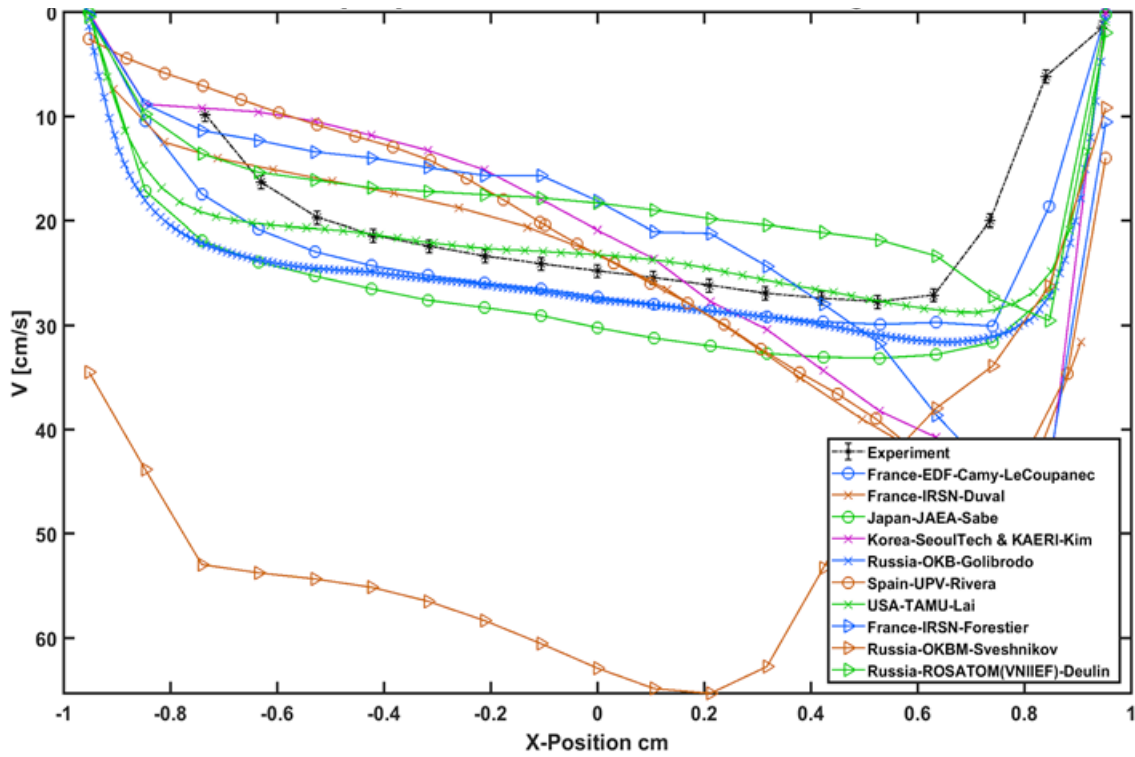
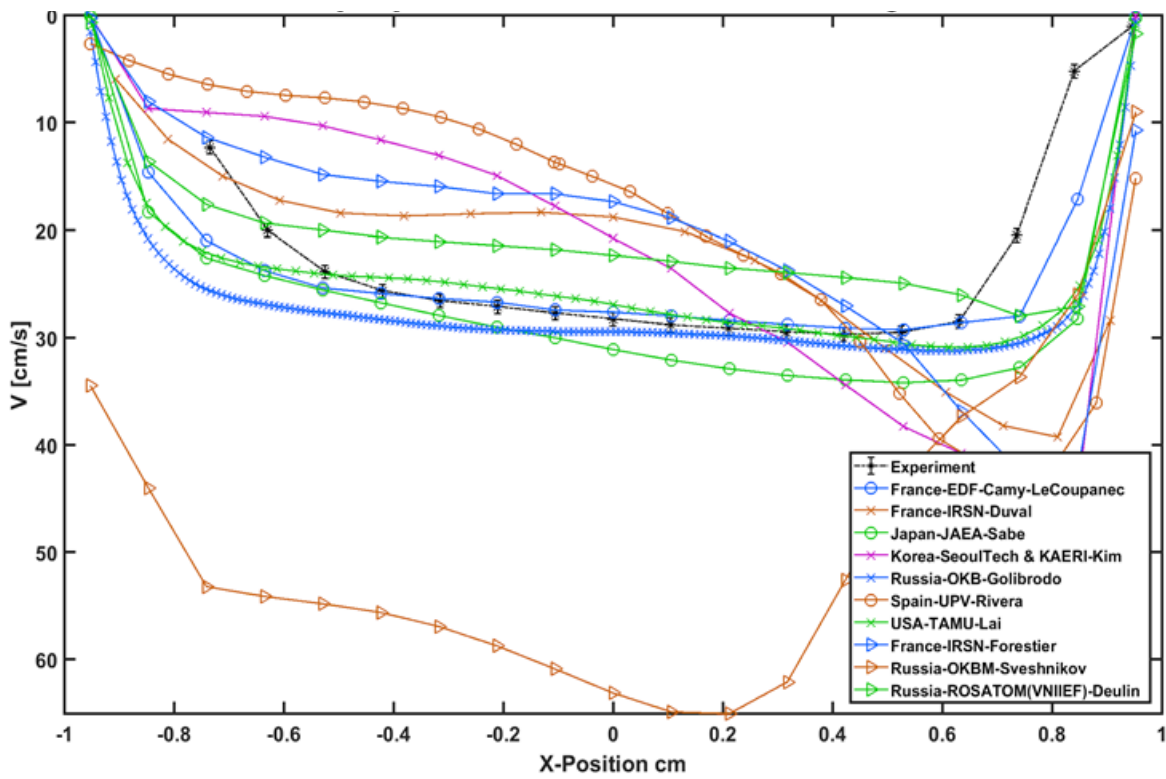


Figure 8.18. V (cm/s) vs. X-position 35.5-41.538 second time-averaged V – DC2



## 9. Synthesis and conclusion

The results of the cold leg mixing benchmark were presented at the third meeting of the WGAMA CFD task group, which took place in Paris, France, on 26 June 2019. In all, 11 teams from 6 countries and 10 institutions submitted results.

Four teams used the same computer code (CFX), while the other remaining teams used eight other different CFD codes. The Large Eddy Simulation was used by eight teams. Three other teams used RANS/URANS techniques for turbulence modelling.

The number of nodes in the CFD mesh varies between about 200 000 (for the coarsest RANS approach) to about half a billion (for the finest LES). Five teams performed an analysis of uncertainties.

The results obtained in the horizontal leg show that:

- All participants predict a stratification of concentrations in the horizontal leg, but a systematic bias is observed for the vertical concentration profile; in all calculation results, the vertical position of this stratification is lower than the measured position and out of the experimental uncertainty range, see Figure 9.4. Most participants predict the correct general shape of the velocity profile as a function of the vertical position; the vertical position of the inflexion point (corresponding to zero horizontal velocity at the boundary between the two fluid layers) is globally well predicted (see Figure 9.1).
- There is significant scattering between participants' results concerning the velocity magnitude in the horizontal leg; most participants predict a velocity magnitude that is higher than the measured value and out of the experimental uncertainty range; a few are close to the experimental results and one participant predicts a lower magnitude of velocity (see Figure 9.3).

The fact that the calculation results give the correct vertical position for the velocity inflexion point, but not for the concentration stratification level, is surprising and should be further investigated. The discrepancy may be due to diffusion. The selection of the Schmidt number tended to match the code predictions well with the experimental data (Lai and Merzari, 2019).

In the downcomer, the comparison of velocity profiles between the inner and outer walls shows significant scattering of calculation results (see e.g. Figure 9.8). The difference with experimental results is quite large, except for the LES computations with the largest number of cells, especially at the beginning of the test; this scattering is lower at later stages of the transient (after 30 s). The difference concerns:

- the vertical flowrate along the measured line, which is related to the prediction of the span width (azimuthal direction along the annulus) of the falling jet;
- the velocity profile shape through the annulus, which directly affects the prediction capability of the CFD for the gradients along the outer wall of the downcomer, this region being of primary relevance for the corresponding safety application.

## References

- Díaz, B., S. Castanedo and P. Palomar (2016), *Experimental characterization of saline density currents generated by brine discharges*.
- Eckstein, A. and P. Vlachos (2009), “Digital particle image velocimetry (DPIV) robust phase correlation”, *Measurement Science and Technology*, Vol. 20. <http://dx.doi.org/10.1088/0957-0233/20/5/055401>.
- Gavelli, F. and K. Kiger (1998), *Experimental investigation of liquid mixing in a complex annular geometry*, American Physical Society, Division of Fluid Dynamics Meeting, November 22-24, 1998 Philadelphia, PA, abstract id. JL.01.
- Lai, J. and E. Merzari (2019), “Sensitivity analyses in a buoyancy-driven closed system with high resolution CFD using Boussinesq approximation and variable density models”, *International Journal of Heat and Fluid Flow*, Vol. 75, pp. 1-13. <https://doi.org/10.1016/j.ijheatfluidflow.2018.11.002>.
- Nguyen, T., N. Goth, P. Jones, S. Lee, R. Vaghetto and Y. Hassan (2017), “PIV measurements of turbulent flows in a 61-pin wire-wrapped hexagonal fuel bundle”, *International Journal of Heat and Fluid Flow*, Vol. 65, pp. 47-59. <https://doi.org/10.1016/j.ijheatfluidflow.2017.03.007>.
- Odier, P., J. Chen and R. Ecke (2014), “Entrainment and mixing in a laboratory model of oceanic overflow”, *Journal of Fluid Mechanics*, Vol. 746, pp. 498-535, <http://dx.doi.org/10.1017/jfm.2014.104>.
- Orea, D., R. Vaghetto, T. Nguyen and Y. Hassan (2019), “Experimental measurements of flow mixing in cold leg of a pressurized water reactor”, *Annals of Nuclear Energy*, Volume 140, 1 June 2020, 107137, <https://doi.org/10.1016/j.anucene.2019.107137>.
- Raffel, M., C. Willert, S. Wereley and J. Kompenhans (2007), *Particle Image Velocimetry: A Practical Guide*, Springer.
- Sciacchitano, A. (2019), “Uncertainty quantification in particle image velocimetry”, *Measurement Science and Technology*, Vol. 30/9. <https://doi.org/10.1088/1361-6501/ab1db8>.
- Timmins, B., B. Wilson, B. Smith and P. Vlachos (2012), “A method for automatic estimation of instantaneous local uncertainty in particle image velocimetry measurements”, *Experimental Fluids*, Vol. 53, pp 1133–1147. <https://doi.org/10.1007/s00348-012-1341-1>.
- Westerweel, J. (1994), “Efficient Detection of Spurious Vectors in Particle Image Velocimetry Data”, *Experimental Fluids*, Vol. 16/3, pp. 236-247. <https://doi.org/10.1007/BF00206543>.

Wilson, B. and B. Smith (2013), “Uncertainty on piv mean and fluctuating velocity due to bias and and random errors”, *Measurement Science and Technology*, Vol. 24/3.  
<https://doi.org/10.1088/0957-0233/24/3/035302>.

Xu, D. and J. Chen (2012), “Experimental study of stratified jet by simultaneous measurements of velocity and density fields”, *Experiments in Fluids*, Vol. 53, pp. 145-162.  
<https://doi.org/10.1007/s00348-012-1275-7>.